Determination of absolute O(3P) and O2(a1Δg) densities and kinetics in fully modulated O2 dc glow discharges from the O2(X3Σg-) afterglow recovery dynamics

Jean-Paul Booth, Abhyuday Chatterjee, Olivier Guaitella, João Santos Sousa, Dmitry Lopaev, S Zyryanov, T Rakhimova, D Voloshin, Yu Mankelevich, Nelson de Oliveira, et al.

Determination of absolute $O(^3P)$ and $O_2(a^1\Delta_g)$ densities and kinetics in fully modulated O_2 dc glow discharges from the $O_2(X^3\Sigma_g^-)$ afterglow recovery dynamics

J-P. Booth[1], A. Chatterjee[1,4], O. Guaitella[1], J. Santos Sousa[2], D. Lopaev[3], S. Zyryanov[3], T. Rakhimova[3], D. Voloshin[3], Yu. Mankelevich[3], N. d'Oliveira[4], and L. Nahon[4]

[1]*Laboratoire de Physique des Plasmas, CNRS, Ecole Polytechnique, UPMC Univ Paris 06, Univ Paris-Sud, 91128 Palaiseau, France*

[2]*Université Paris-Saclay, CNRS, Laboratoire de Physique des Gaz et des Plasmas, 91405 Orsay, France*

[3]*Skobeltsyn Institute of Nuclear Physics, Lomonosov Moscow State University, Russian Federation*

[4] *Synchrotron SOLEIL, L'Orme des Merisiers, Saint Aubin BP 48, 91192 Gif-sur-Yvette Cedex, France*

Abstract

A method is presented for the determination of the absolute densities of $O(^3P)$ atoms and $O_2(a^1\Delta_g)$ molecules in an O_2 electrical discharge, which does not depend on any calibration procedure or knowledge of optical transition strengths. It is based on observing the recovery dynamics of the $O_2(X^3\Sigma_g^-)$ density in the afterglow of a fully-modulated discharge, and is demonstrated in a dc glow discharge in pure O_2 at pressures of 0.2-4 Torr. The time-resolved $O_2(X^3\Sigma_g^-)$ density was measured by VUV absorption spectroscopy using the monochromator branch of the VUV DESIRS beamline at Synchrotron SOLEIL, but this methodology could be used with another density measurement technique. During the active discharge, the $O_2(X^3\Sigma_g^-)$ density is depleted by a combination of O_2 dissociation, excitation into metastable states (principally $O_2(a^1\Delta_g)$) and gas heating/dilation. After discharge extinction, the $O_2(X^3\Sigma_g^-)$ density progressively recovers to its initial (before discharge) value, with three distinct time-constants due to: i) gas cooling (fast), ii) $O(^3P)$ atom recombination (intermediate), and iii) $O_2(a^1\Delta_g)$ quenching (slow). The $O(^3P)$ and $O_2(a^1\Delta_g)$ dynamics can be separated easily, allowing the $O(^3P)$ and $O_2(a^1\Delta_g)$ afterglow loss kinetics to be determined, as well as their mole fractions in the steady-state discharge. Both the $O(^3P)$ and $O_2(a^1\Delta_g)$ mole-fractions increase with current (up to the highest current studied, 40 mA) and pass

through maxima with pressure at 1 Torr, reaching 16.5% and 8%, respectively. $O(^3P)$ atoms are principally lost by recombination at the borosilicate tube surface, with a loss probability in the afterglow of $\sim 8 \cdot 10^{-4}$, nearly independent of gas pressure and discharge current (in contrast to previous observations in the active discharge [1] . The $O_2(a^1\Delta_g)$ dynamics were also measured by IR emission spectroscopy. In the late afterglow this agrees well with the $O_2(X^3\Sigma_g^-)$ recovery dynamics, corresponding to an $O_2(a^1\Delta_g)$ surface loss probability of $\sim 2.2 \cdot 10^{-4}$. The initial $O_2(a^1\Delta_g)$ loss is faster than in the later afterglow, indicating that it is also quenched by O atoms.

1. Introduction

Low-temperature gas discharge plasmas enable many modern technologies, notably material processing (especially for microelectronics), and are becoming increasingly important in medicine, biology and agriculture. These applications depend on the ability to produce high concentrations of reactive neutral particles, notably free radicals and especially atoms, of which oxygen is one of the most widespread and important. Controlling and optimizing these processes requires understanding of the detailed reaction mechanisms and accurate measurements of the rate constants, which in turn depends on accurate measurements of reactive atom concentrations. Several methods have been developed to measure the density of ground-state oxygen atoms occurring in flames, discharges and afterglows. Nevertheless, these methods (which we will review below) each have disadvantages, limitations in applicability or questionable accuracy. They all depend upon parameters (such as line strengths, quenching rates and excitation cross-sections) which must be determined in separate experiments, themselves often dependent on further external data. Some only provide estimates of volume-averaged concentrations, when in many practical situations the studied species has a strongly non-uniform spatial distribution.

Chemical titration using NO molecules has historically been considered to be the reference technique for oxygen atom density measurements [2-5]. The three-body recombination reaction: $O(^3P) + NO + M \rightarrow NO_2^* + M$ can be followed through the chemiluminescence, and the flux of $O(^3P)$ atoms entering the titration zone is then assumed to be equal to the flux of NO molecules needed to saturate the chemiluminescence intensity. However, the accuracy of this method depends on many parameters, including the initial spatial distribution of the atoms, the mixing dynamics of the gas flows, and the position where the NO_2^* emission is observed. Often the oxygen-containing sample is expanded into a large, low-pressure volume for the titration, which can lead to errors of a factor of 2 - 3 without detailed 2D or 3D modelling [2,6]. Even then, the

error bars remain significant, in part due to uncertainty in the reaction rate constants used in these models.

Threshold-ionization mass-spectrometry has also been used to estimate the absolute density of oxygen atoms in plasmas [7]. However, this technique requires knowledge of (i) Atomic ionization cross-sections near threshold, whose accuracy is rather limited. (ii) Instrumental parameters, including the rates of recombination of atoms on the internal walls of the spectrometer and ionizer filament. Furthermore, atom recombination on the sampling structure can considerably perturb the measured atom density.

Optical methods have the advantage that they do not perturb the plasma, and allow localized density measurements with high temporal resolution. The simplest method, at least in terms of the required equipment, is optical emission actinometry [5,8-20], where the emission intensity from excited states of oxygen atoms is compared to the emission intensity from an excited state of an inert actinometer gas (generally a noble gas, e.g. Ar) added in known quantity. The ratio of these intensities is then assumed to be proportional to the ratio of the two species' number densities. The proportionality coefficient is a function of the ratio of the electron-impact excitation rate constants of the emitting atoms, as well as other plasma parameters. With an appropriate choice of emitting states (most importantly, having energy thresholds for electron-impact excitation that are relatively close), the ratio of the excitation rate constants mainly depends on the excitation cross-sections near the threshold. Unfortunately, these cross-sections are extremely difficult to measure for a transitory species and with an absolute scale. For oxygen atoms the semi-empirical cross-sections of Laher and Gilmore [21] have been widely used. More recently, sophisticated *ab-initio* calculations have been made [22], but these cross-sections have not been confirmed experimentally, and do not include collisional cascade contributions that may be significant in experimental situations. Additionally, if the plasma is spatially non-uniform the geometry of the emission collection can have a significant impact in the results.

The Two-photon Absorption Laser-Induced Fluorescence (TALIF) technique is widely used for $O(^3P)$ density measurements, due to its good sensitivity, high spatial and temporal resolution, independence from electronic excitation calculations, and its applicability to atmospheric-pressure discharges [5,15-17,23-30, 31]. In its initial implementation, TALIF only provides *relative* density measurements. In 1998 Goehlich et al. [26] proposed a method to obtain absolute densities of H, N and O atoms from TALIF by calibrating the signal against TALIF of a known quantity of a rare gas (Xe in the case of O atoms). This technique was further developed and refined in later publications [23-25]. Crucially, this calibration depends on the ratio of the two-photon excitation cross-sections for the oxygen and xenon transitions used. This ratio has only

been determined a few times, using titration as the reference [24-26], or even actinometry [5,15,17]. Furthermore, it is necessary to make fastidious measurements of the laser intensity-dependence curves for both species (O and Xe) over two orders of magnitude to confirm the quadratic regime, and to determine the wavelength dependency of the detection sensitivity, both of which add uncertainty to the measurement. Given these sources of uncertainty, we estimate that the absolute accuracy of this method is not much better than a factor of about 2. Indeed, absolute TALIF measurements at our laboratory in a similar discharge tube provided physically unrealistic atom densities in some circumstances, approaching or exceeding the total gas density determined from the ideal gas law.

Absorption-based methods are attractive for absolute density measurements, since the Beer-Lambert law is intrinsically self-calibrating. Provided that the density distribution is uniform along the absorption path (as is the case for a cold gas), or can be determined independently, the only source of uncertainty (apart from measurement noise) is the accuracy with which the optical transition probabilities are known. These can be measured easily for stable molecules, but this is more difficult for transitory atoms and free radicals. In this case one has to either: 1) measure the absorption of a known density of the species in question (therefore relying on another calibration technique), 2) measure the fluorescence lifetime of the upper level in a pulsed experiment (only possible for allowed transitions), and convert to absorption via the Einstein relation, or 3) Use *ab-initio* calculations. For allowed transitions in atoms, ab-initio calculations are well-developed, and pulsed fluorescence experiments are also feasible, so these transition strengths are often known with high accuracy. This is the case for the well-known allowed $O(2p^4\ ^3P_J) \rightarrow O(^3S_1^o)$ resonant transitions of $O(^3P)$ atoms around 130 nm. However, this transition is so strong that the absorption at the line center is so high that saturation is reached even for very small atom concentrations ($<10^{13}$ cm^{-3} along the line of sight), limiting its use to very low concentration (such as very short discharge pulses [32], low-pressure plasmas [33] or very small objects [34,35]). Furthermore, vacuum ultraviolet light is difficult to work with, and laboratory-sized spectrometers do not permit Doppler resolution. Commonly a resonance lamp is used as the light-source. In this case it is necessary to measure (or estimate) the spectral profiles of both the light source and the absorber, and calculate the "curve of growth" to obtain the atom density, adding greatly to the uncertainty of the measurement [32,33]. Use of synchrotron-generated VUV light, combined with a high-resolution Fourier-transform spectrometer, has recently been demonstrated, allowing Doppler resolution [34,35]. Nevertheless, this technique is limited to low values of the line-integrated density.

An alternative for the detection of $O(^3P)$ atoms is to measure the forbidden $O(2p^4\ ^3P_2) \rightarrow O(2p^4\ ^1D_2)$ absorption transition at 630 nm. In this case the absorption is so low that cavity-enhanced methods are necessary, such as intra-cavity laser absorption spectroscopy (ICLAS) [36], cavity-enhanced absorption Spectroscopy (CEAS) [37,38], and cavity ring-down spectroscopy (CRDS) [39,40]. One complication with cavity-enhanced techniques is that delicate high-reflectivity mirrors are needed. These are usually positioned on long arms away from the active plasma, in order to prevent their degradation, leading to uncertainty in the atom density profile along the absorption path. In addition, *ab-initio* calculations are more challenging for forbidden transitions, so the line-strengths are known with less precision. For the $O(2p^4\ ^3P_2) \rightarrow O(2p^4\ ^1D_2)$ transition the claimed uncertainty in the calculated line-strength is ≤7% [41]. Nevertheless, an independent experimental validation of this theoretical line-strength is necessary before absolute densities can be stated with confidence.

In summary, no existing method to measure $O(^3P)$ density can guarantee absolute accuracy better than and few 10's %. A more accurate method, independent of external calibrations or parameters, is highly desirable. Firstly, this would permit the validation (for relative trends), and calibration (for absolute values), of the other existing methods (actinometry, TALIF, and CRDS), which may be more appropriate or convenient to use in specific discharges. Secondly, accurate absolute density measurements are required for the determination of accurate reaction rate constants, and for the validation of discharge models.

Analogous concerns apply to the measurement of oxygen molecules in the metastable singlet delta ($O_2(a^1\Delta_g)$) state. The absolute $O_2(a^1\Delta_g)$ density has been determined from the very weak infrared emission back to the $O_2(X^3\Sigma_g^-)$ ground state. This transition is doubly forbidden (the Einstein A coefficient is only $2.256\text{x}10^{-4}s^{-1}$), although in this case the line strength has been measured with high accuracy by cavity-enhanced absorption measurements on high densities of ground-state O_2 gas [42,43]. Absolute intensity measurements of such weak emission, from a diffuse (plasma) source, are difficult, so it is hard to obtain accuracy better than about -30%/+50%. $O_2(a^1\Delta_g)$ molecules have also been detected by absorption to the $O_2(b^1\Sigma_g^+)$ state (the Noxon band), but this is again very weak, necessitating intra-cavity absorption spectroscopy methods (CRDS [44-47] or ICLAS [48]). The strength of this transition has never been measured, so it is only known from ab-initio calculations. $O_2(a^1\Delta_g)$ molecules also show several strong absorption bands in the VUV spectral region [48]. These include sharp transitions to high Rydberg states [49] as well as diffuse bands to repulsive states, such as the wide band around 128.5 nm used in several previous studies of $O_2(a^1\Delta_g)$ in O_2 plasmas [50, 31] . The VUV absorption cross-section of $O_2(a^1\Delta_g)$ has been measured only once, by Ogawa and Ogawa, in 1975 [48]. In this work, the magnitude of

the cross-section depends upon an estimate of the $O_2(a^1\Delta_g)$ density in the absorption cell. The transitions from $O_2(a^1\Delta_g)$ to Rydberg states were recently revisited [49], both experimentally and by ab-initio calculations of the absolute transition strengths. This work suggests that the Ogawa and Ogawa cross-sections should be increased by a factor of about 1.5. Therefore, as for atomic oxygen, a method for absolute $O_2(a^1\Delta_g)$ density determination that is independent of calibration and other external parameters is also highly desirable.

The positive column region of a dc glow discharge provides excellent plasma uniformity along the discharge axis, making it ideal for absorption measurements. The discharge is less uniform in the radial direction, due to the presence of gas temperature gradients. These become stronger at higher discharge currents and gas pressures [1], leading to a radial gradient in the total gas density, N. The tube walls play a significant role in the losses of $O(^3P)$ atoms and $O_2(a^1\Delta_g)$ molecules. Nevertheless, the surface loss probabilities for both species are small (for borosilicate glass they are 10^{-3} [1] and ~10^{-4} [51-53] respectively), so that the mole-fractions ($O(^3P)/N$ and $O_2(a^1\Delta_g)/N$, where N is total gas density) are quite uniform. The radial density profiles of these two species will therefore follow the total gas density profile, which is inversely proportional to the gas temperature profile.

This study presents a new method, independent of external calibrations and coefficients, to measure $O(^3P)$ atom and $O_2(a^1\Delta_g)$ molecule densities. The principle of this method is to observe the recovery dynamics of the initial $O_2(X^3\Sigma_g^-)$ density in the afterglow of a fully-modulated discharge, under conditions when the loss time constants of $O(^3P)$ and $O_2(a^1\Delta_g)$ are distinctly different, and are long compared to the charged particle lifetimes. This is the case in relatively low gas pressure (< 10 Torr) discharges in pure O_2, where gas-phase reactions are slow, and when the surface material is such that the surface losses probabilities are relatively small. When the discharge is switched on, the $O_2(X^3\Sigma_g^-)$ number density is depleted due to O_2 dissociation, as well as excitation into metastable states (mainly $O_2(a^1\Delta_g)$, and some $O_2(b^1\Sigma_g^+)$) and gas heating. After switching off, the $O_2(X^3\Sigma_g^-)$ number density progressively recovers to the initial (before discharge) value. The recovery rate is determined by the different processes occurring: i) gas cooling, ii) $O_2(b^1\Sigma_g^+)$ quenching, iii) $O(^3P)$ atom recombination, and iv) $O_2(a^1\Delta_g)$ quenching. Under the conditions studied here, the fastest process is gas cooling and $O_2(b^1\Sigma_g^+)$ quenching, after which the loss processes of the remaining transient species can be separated in time. This allows the determination of the mole fractions of $O(^3P)$ atoms and $O_2(a^1\Delta_g)$ molecules. The method is demonstrated on the positive column of a dc glow discharge in O_2 operated in a borosilicate tube at pressures up to 4 Torr. The dynamics of the $O_2(X^3\Sigma_g^-)$ number density were measured by VUV

absorption spectroscopy. In parallel, the $O_2(a^1\Delta_g)$ concentration dynamics were followed by IR emission spectroscopy, and the $O(^3P)$ atom density (more exactly the mole fraction $[O(^3P)]/N$) was also determined by the actinometry method.

Section 2 describes the experimental setup and the diagnostics used. Section 3 presents the results obtained and their discussion.

2. Experiment

2.1 Discharge Tube.

The experimental setup is shown schematically in Figure 1. The discharge tube, similar to that used by Booth et al. [1], is made of borosilicate glass (thickness 2 mm) with an inner diameter of 20 mm. The electrodes are situated in side-arms (~30 mm long, diameter ~10 mm), separated by 525 mm, so that only the positive column is observed in the main tube. The electric field in the positive column was measured by two high-impedance floating probes, as described previously [1]. The tube surface temperature was kept constant at 50°C by a water/ethanol mixture flowing through an outer envelope and connected to a thermostatic bath. The temperature drop across the tube wall is estimated to be less than 2 K for the linear power loading (≤ 1 Wcm^{-1}) used here. The anode is connected to a positive-polarity high-voltage power supply via two serial 68 kΩ ballast resistors, and the cathode is connected to ground via a non-inductive 15 kΩ ballast resistor. For full-modulation measurements, a high-voltage switch (Belke) was used to turn the discharge on and off. For partial-modulation measurements, the 15 kΩ ballast resistor connecting the cathode to ground was short-circuited with a power FET.

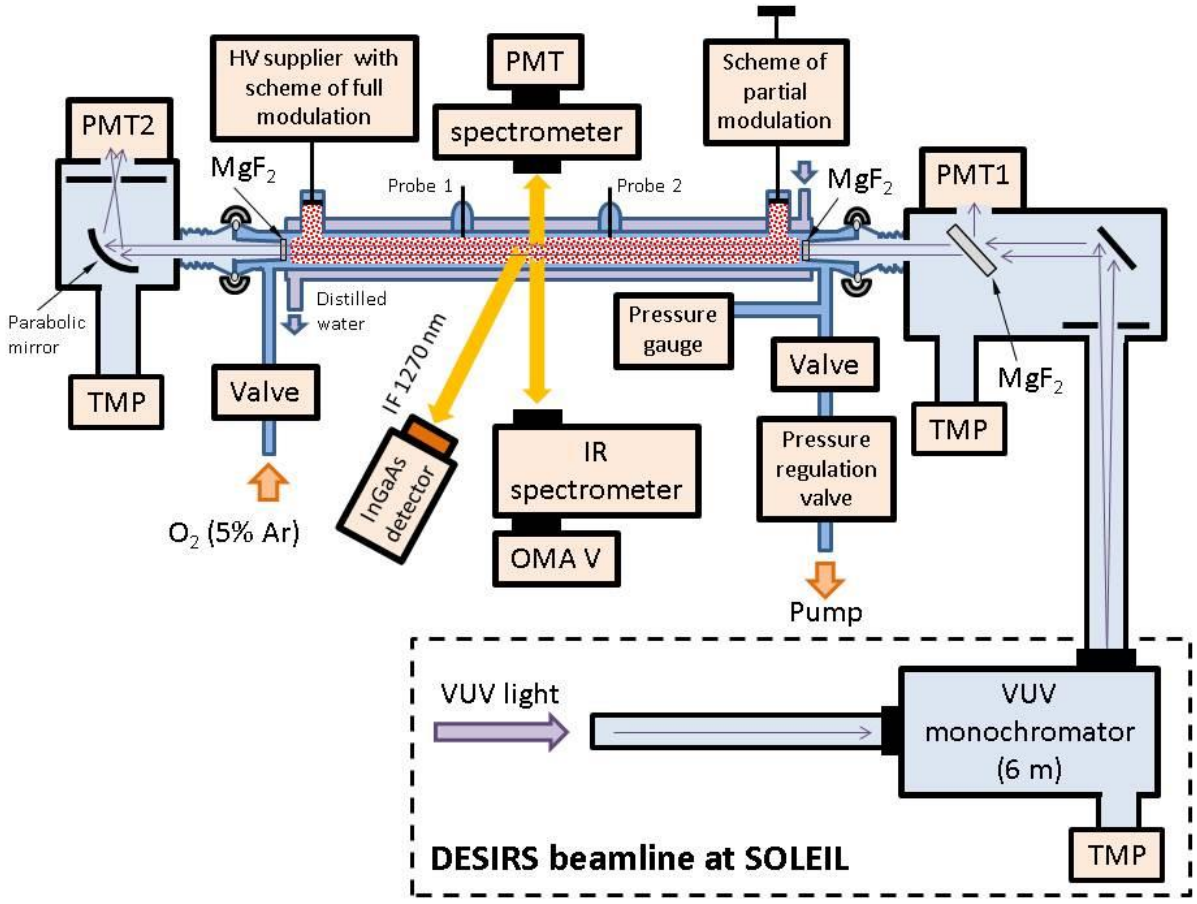

Figure 1. Experimental setup showing the DC discharge set-up connected to the DESIRS VUV beamline (for VUV absorption measurements), along with the other diagnostics. PMT stands for photomultiplier, TMP for turbomolecular pump.

O_2 gas (99.9995% purity) and Ar (5% of total gas flow) was supplied via mass flow controllers to one end of the tube, and evacuated from the other end by an oil-free scroll pump via a manual regulation valve. The pressure was measured by a 10 Torr capacitance manometer, situated between the discharge tube and the pressure regulation valve. The accuracy of the pressure measurements was checked by measuring the Schumann-Runge VUV absorption of a pure O_2 gas without discharge and using the absorption cross-sections of Gibson et al. [54], giving agreement within 1%. Measurements were made in O_2 discharges over the pressure range 0.2-4 Torr and for currents of 10-40 mA. The gas flow was kept small (flow rate of 2 sccm for pressures <1 Torr and 5 sccm for pressures >1 Torr), so that the gas residence time was longer than the lifetime of all transient species created in the discharge. Simultaneous measurements of the $O(^3P)$ mole-fraction (by optical emission actinometry) and of the $O_2(a^1\Delta_g)$ density (from the 1268 nm IR emission) were made in continuous discharges. The gas temperature, averaged over the tube cross-section, was determined from the rotational structure of the O_2 A-band ($O_2(b^1\Sigma_g^+, v=0) \rightarrow O_2(X^3\Sigma_g^-, v=0)$) emission around 760 nm [55]. The loss kinetics of $O(^3P)$ and $O_2(a^1\Delta_g)$ in the active discharge were

determined by time-resolved optical emission measurements in partially-modulated discharges [9].

Full-modulation experiments were performed in pure O_2, with the discharge on for 200 ms and off for 800 ms, which is long enough to allow the $O_2(X^3\Sigma_g^-)$ density to reach steady values in each case. We simultaneously measured the time-resolved $O_2(X^3\Sigma_g^-)$ density (by VUV absorption) and the $O_2(a^1\Delta_g)$ density (by 1268 nm IR emission). In full-modulation experiments the gas flow was stopped by pneumatic valves (on the entrance and exit tubes) immediately prior to the measurements. This was done to keep the total number of oxygen atoms in the tube (in both atomic and molecular forms) constant during the pulsing cycle. The valves were closed with the discharge running, so that the pressure in the tube during the discharge-on period is equal to that in a flowing, continuous discharge. Conversely, the pressure in the sealed tube when the discharge if off is lower than the nominal pressure. Even if we cannot measure this pressure directly (the pressure gauge is situated outside this region), it can be determined it from the density of the cold O_2 in the late afterglow (measured by the $O_2(X^3\Sigma_g^-)$ VUV absorption).

2.2. $O_2(X^3\Sigma_g^-)$: VUV absorption measurements.

Experiments were performed on branch B of the DESIRS Vacuum Ultraviolet beamline [56] at synchrotron SOLEIL. Broadband VUV synchrotron radiation from the undulator passes through a 6.65 m VUV monochromator, producing a tunable narrow-band beam. Higher harmonics from the undulator are suppressed by the presence of MgF_2 windows (cut-off around 10.6 eV). Using the 200 lines/mm grating and a slit width of 200 microns gave a spectral bandwidth of ~0.14 nm at wavelengths around 170 nm (6 meV @ 7.3 eV). Much higher spectral resolution is possible on this beamline (up to $\delta\lambda/\lambda \approx 5{\cdot}10^{-6}$), but at the cost of greatly reduced photon flux. Since we are studying the continuum region of the $O_2(X^3\Sigma_g^-)$ spectrum, high spectral resolution was not required; additionally, it is important to have a high synchrotron photon flux compared to the discharge VUV emission (predominantly the oxygen atom 130 nm resonance lines), which can only be achieved at lower resolution. The VUV beam is focused to a point just before entering the discharge tube (beam size about 70 by 200μm), and diverges to about 3x6 mm at the exit. This is still much smaller than the 20 mm inner diameter of the discharge tube. Before entering the discharge tube, the beam is sampled by a 45° MgF_2 (uncoated) beam-splitter, and the intensity of this reference beam was monitored by a visible photomultiplier, PMT1, behind a sodium salicylate scintillator. The transmitted beam passes along the axis the discharge tube, and is then focused by a parabolic mirror through a diaphragm (to reduce parasitic light from the discharge) and detected

by a solar-blind photomultiplier, PMT2. The discharge region was separated from the high-vacuum regions by MgF_2 windows mounted on re-entrant conical Pyrex inserts, as shown in Figure 1. The distance between the MgF_2 windows was 615 mm, so that the positive column almost touches the windows.

The density of oxygen molecules in the $O_2(X^3\Sigma_g^-)$ ground state was determined from the continuum absorption (for photon energies above ~7.08 eV) in the long-wavelength shoulder of the Schumann-Runge band. At higher gas pressures, it was necessary to move to progressively longer wavelengths (where the absorption cross-section is smaller) to obtain adequate transmitted signal intensity on PMT2. Figure 2 shows the relevant part of the O_2 absorption spectrum, measured in flowing pure O_2 gas without a discharge by scanning the VUV monochromator wavelength. The observed absorption cross-sections agreed with Gibson et al. [54] to within 1%, attesting to the accuracy of the pressure measurement. The arrows indicate the photon energies used for the different pressures. The lowest photon energy (longest wavelength) used was 7.1 eV (for pressures of 3 and 4 Torr). The O_2 absorption cross-section in this spectral region increases with the gas temperature, especially at the lowest photon energies used [54, 57]. However, we only used kinetic data from the later afterglow, when the gas temperature has equilibrated to the tube temperature (set at 323 K).

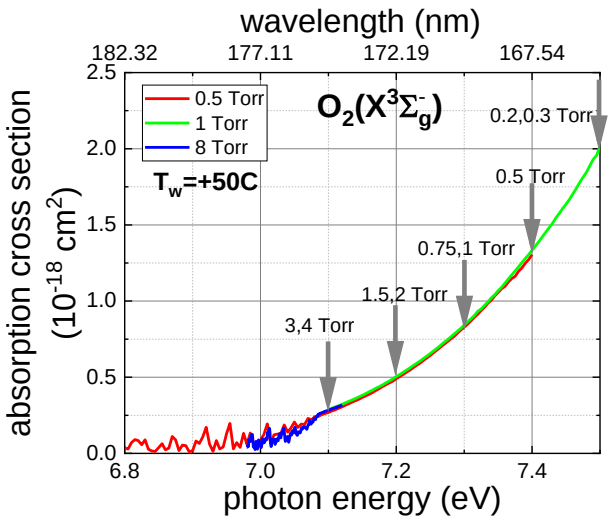

Figure 2. Measured absorption cross-section of ground state $O_2(X^3\Sigma_g^-)$ in the long-wavelength shoulder of the Schumann-Runge band at 323 K. The arrows indicate the photon energies used for different pressures.

2.2. $O_2(a^1\Delta_g)$: IR emission measurements.

$O_2(a^1\Delta_g)$ molecules were detected by the $O_2(a^1\Delta_g, v=0) \rightarrow O_2(X^3\Sigma_g^-, v=0)$ emission around 1268 nm. This emission was detected using two different setups, as described by Santos Sousa and

Puech [31]. In the first setup, an InGaAs photodiode (Judson J22D-M204-R03M-1.7, with a 10^9 V/A transimpedance amplifier) equipped with an interference filter (1272 nm, bandwidth ~19 nm FWHM) was placed at a distance of ~10 cm from the tube axis, without any lens. This setup does not allow spectral resolution of the emission, but has good temporal resolution (~0.5 ms), allowing the $O_2(a^1\Delta_g)$ dynamics to be followed during discharge modulation.

In the second setup, light emitted by the discharge was collected by a lens (focal length 50 mm, diameter 25mm), situated on the opposite side of the tube to the photodiode, and focused into a 2-metre optical fibre. The light from this fibre was injected into a 300 mm focal-length IR spectrograph (Acton SP-2300i) equipped with a liquid nitrogen-cooled InGaAs 512-element linear photodiode array (Princeton Instruments OMA-V). This allowed the emission spectrum from continuous discharges to be spectrally resolved.

Examples of the emission spectra are shown in Figure 3, for 20 mA current and pressures of 0.5, 1, 2 and 4 Torr. At pressures below 1 Torr, in addition to the $O_2(a^1\Delta_g)$ emission, two O atom lines are also observed, becoming stronger at lower pressures. This is because the reduced electric field, E/N, is higher at lower pressure, which enhances the O atom excitation (excitation energy E_{exc} > 13 eV) relative to $O_2(a^1\Delta_g)$. Nevertheless, the O atom contribution to the total observed intensity remains small for all conditions studied here.

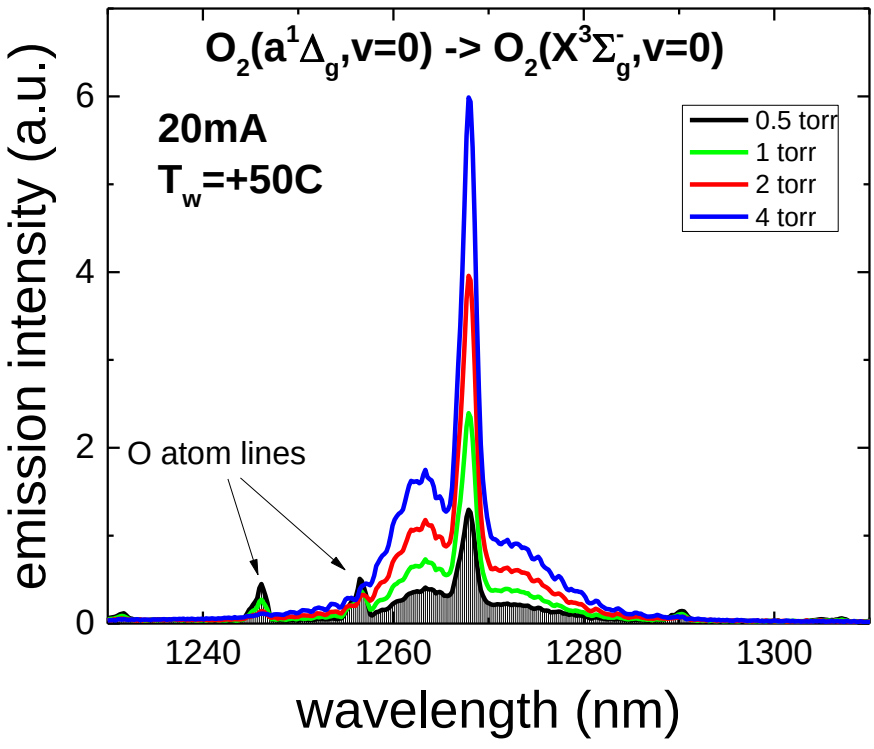

Figure 3. Examples of measured $O_2(a^1\Delta_g)$ IR emission spectra for different pressures at a current of 20 mA. The spectral resolution is ~0.55 nm.

To deduce the absolute $O_2(a^1\Delta_g)$ density (averaged over the tube cross-section) from these measurements, it is necessary to know the absolute sensitivity of both detection systems. This was accomplished differently for the two setups. For the photodiode setup no lenses were used, and the observed emitting volume was limited axially (Δz = 2 cm) by two black cards in order to fulfill the condition $L >> \Delta z$ (where L is the distance of the detector from the tube axis), but large enough to provide an adequate signal level. Assuming that $L >> R_{tube}$, the $O_2(a^1\Delta_g)$ density can then be deduced directly from the measured detector current, I_{det}, from the following formula:

$$[O_2(a^1\Delta_g)] = \frac{4\pi L^2 \cdot I_{det}}{h\nu \cdot A \cdot S_{det}\eta_{f.det}V},$$

where $h\nu/e$= 0.98 eV, A = $2.256\cdot10^{-4}$ s^{-1} is the Einstein coefficient for the transition, S_{det} is the surface area of the detector, $\eta_{f.det}$ is the product of the detector sensitivity (0.88 A/W at 1270 nm, from the manufacturer's data sheet) by the transmission of the interference filter (34 % transmission at 1270 nm), and $V=\Delta z.\pi R_{tube}^2$ is the emitting volume. These measurements were made at higher gas pressures, where the intensity of parasitic O atom emission can be neglected. Measurements were made at three different detector distances (L = 10, 14 and 17 cm), in order to estimate the uncertainty of the measurement.

For the second configuration, the absolute sensitivity of the spectrograph + array detector was estimated by observing the oxygen atom emission at 845 nm simultaneously with the spectrograph system and with an absolutely-calibrated Si detector. The AXUV100 silicon photodiode, surface area S_{det} =1 cm^2, was situated at a distance, L, from the tube axis ($L >> R_{tube}$) located behind an 845 nm interference filter. The relative sensitivity (1268 nm/845 nm) of the spectrograph and photodiode array was corrected using the manufacturer's data. The absolute intensity of the oxygen atom emission at 845 nm, P_{O845} was calculated from the photodiode current, I_{det}, (similarly to the case of the InGaAs photodiode), from:

$$P_{O845} = \frac{4\pi L^2 \cdot I_{det}}{S_{det}\eta_{f.det}},$$

where $\eta_{f.det}$ is the product of the photodiode sensitivity (0.44 A/W at 845 nm, from the supplier's data sheet) by the transparency of the interference filter (60 % at 845 nm with bandwidth ~10 nm FWHM). We can then deduce the absolute $O_2(a^1\Delta_g)$ density from the ratio of the spectrally-integrated intensities of the O atom 845 nm line and the $O_2(a^1\Delta_g)$ 1270 nm band observed with the spectrograph, $\int I_{O845}d\lambda$ and $\int I_{O2(a)}d\lambda$, respectively, from the following formula:

$$[O_2(a^1\Delta_g)] = P_{O845}\frac{\int I_{O2(a)}d\lambda}{\int I_{O845}d\lambda}\cdot\frac{\eta_{845}}{\eta_{1270}}\cdot\frac{1}{h\nu_{845}\cdot A_{845}\cdot V}$$

,

where $h\nu_{845}$/e= 0.98 eV, A_{845} = 2.256·10^{-4} is the Einstein coefficient for the transition, *V* is the emitting volume (the same as in the first calibration), and η_{845} and η_{1270} are convolutions of the photodiode array sensitivity with the reflectivity of the spectrograph mirrors and grating (which for the Acton SP-2300i are almost the same at 845 and 1270 nm).

The two techniques gave comparable results, although the InGaAs photodiode/interference filter technique gave $O_2(a^1\Delta_g)$ densities about 40% higher. Some of this difference could be due to a contribution by O atom emission to the InGaAs photodiode signal, as seen in Figure 3. The monochromator calibration could also be an underestimate, due to the fact that the O atom emission is more strongly peaked at the tube axis where the reduced field is strongest, whereas the $O_2(a^1\Delta_g)$ density (and emission intensity) is higher nearer the walls where the gas is cooler and denser.

2.3. O(^{3}P): Actinometry measurements.

Actinometry measurements were made by adding 5% of Ar to the O_2 flow. This has been shown to have no significant effect on the discharge parameters or the densities of active neutrals such as O(^{3}P) atoms and $O_2(a^1\Delta_g)$ molecules [10,16-18]. The standard emission lines were used: Ar($2p_1$) at 750 nm, O($3p^5$P) at 777 nm and O($3p^3$P) at 845 nm. The excitation rate constants of the lines were calculated using recent *ab-initio* calculations of the excitation cross sections for O atoms [22] and for Ar [58]. Using this technique we measured both the O(^{3}P) density in continuous discharges, and the O(^{3}P) loss frequencies in the active discharge by time-resolved actinometry during partial modulation of the discharge current [1].

3. Results

3.1 $O_2(a^1\Delta_g)$ kinetics

Examples of the temporal behavior of the $O_2(a^1\Delta_g)$ density during full modulation of the discharge (from the IR emission) are shown in Figures 4a and 4b, for pressures of 1 Torr and 4 Torr respectively. The $O_2(a^1\Delta_g)$ density reaches steady state well before the end of the 200 ms discharge period. At 4 Torr there is a small, fast increase of the $O_2(a^1\Delta_g)$ density immediately after switching off the discharge (Figure 4b), which can be explained by the return of gas (containing $O_2(a^1\Delta_g)$) from the region near the walls to the tube axis as it cools. Subsequently, the $O_2(a^1\Delta_g)$ density

decays. However, the decay is not single-exponential, being somewhat faster in the early afterglow (up to around 100 ms). The amplitude of this initial faster decay component increases both with discharge current and with gas pressure, indicating that the absolute density of the species causing this additional $O_2(a^1\Delta_g)$ loss also increases with current and pressure. The only species present in significant quantities showing such behavior are O (^{3}P) atoms (see below). Therefore the faster initial decay of $O_2(a^1\Delta_g)$ can be explained by quenching by O(^{3}P) atoms. Dvoryankin et al. [59] estimated a rate constant $k_q \approx 7.6 \cdot 10^{-16}$ cm^3/s for this process. Although the density of O atoms is one order of magnitude lower than that of O_2, this rate constant is ~700 x bigger than that for O_2, so this process is two orders of magnitude faster overall. The fraction of $O_2(a^1\Delta_g)$ molecules lost through this process reaches up to 25% of the total $O_2(a^1\Delta_g)$ at the highest pressure and current (4 Torr 40 mA), but is smaller under all other conditions.

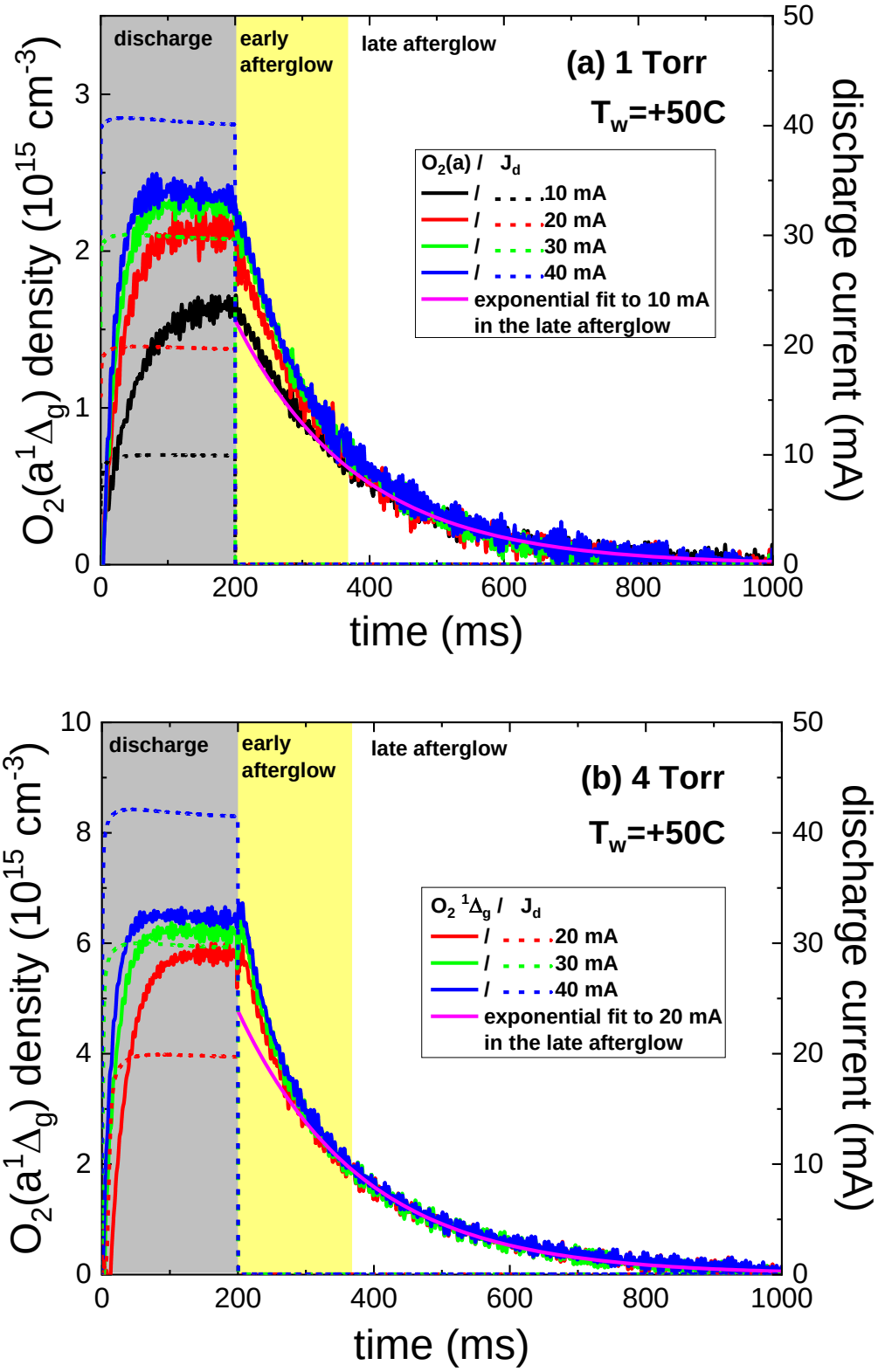

Figure 4. Examples of the $O_2(a^1\Delta_g)$ density dynamics (from IR emission) during full modulation of the discharge (discharge duration – 200 ms, afterglow duration – 800 ms). (a) 1 Torr and (b) 4 Torr. The magenta curve is a single-exponential fit for the $O_2(a^1\Delta_g)$ decay in the late afterglow for 10 mA in 1 Torr (a) and 20 mA in 4 Torr (b). The dashed curves correspond to the temporal evolution of the discharge currents.

After the initial period, the $O_2(a^1\Delta_g)$ density decays exponentially with a slower loss frequency, $\nu_q^{O2(a)}$. Figure 5 shows how this loss frequency varies with plasma conditions. With pressure it passes through a minimum (around 1.5 Torr), and with discharge current it increases slightly, even though these measurements were made in the afterglow. First, let us discuss the small increase with pressure above 1.5 Torr (corresponding to an increase rate of ~ 0.33 s^{-1}/Torr), which can be explained by gas-phase processes. It is known that $O_2(a^1\Delta_g)$ is quenched by collision with ground-state O_2 molecules:

$$O_2(a^1\Delta_g) + O_2 \rightarrow O_2 + O_2 \qquad k_q^{O2} = 2.2 \cdot 10^{-18} \cdot \left(\frac{T_g}{300}\right)^{0.8} \text{ cm}^3/\text{s} \quad [60]$$

However, at 323 K this gives $k_q^{O2} = 1.61 \cdot 10^{-18}$ cm^3/s, or only about 0.05 s^{-1}/Torr, so this cannot account for the major part of the observed increase with pressure. Another possibility is the presence of small amounts of ozone. Ozone has been shown to quench $O_2(a^1\Delta_g)$ much more efficiently:

$$O_2(a^1\Delta_g) + O_3 \rightarrow O + O_2 + O_2 \qquad k_q^{O3} = 5.1 \cdot 10^{-11} \cdot e^{-\frac{2840}{T_g}} \text{ cm}^3/\text{s} \quad [61].$$

At 323 K, this gives $k_q^{O3} = 7.74 \cdot 10^{-15}$ cm^3/s, so that the observed increase of $\nu_q^{O2(a)}$ with pressure above 1.5 Torr could be explained by an ozone concentration of the order of $1.5 \cdot 10^{14}$ at 4 Torr (~0.1% of the gas phase). This value is very comparable to that measured in the afterglow in a similar discharge by Marinov et al. [62]. Note that (as shown by Marinov et al.) the ozone density in the active discharge is much lower than this due to the existence of rapid destruction processes).

The minimal $O_2(a^1\Delta_g)$ loss frequency is ~5 s^{-1}, which corresponds to a surface loss probability of $\gamma_{O2(a1\Delta g)} \approx 2.2 \cdot 10^{-4}$. This is very comparable to literature values for Pyrex and quartz [51-53]. Now let us consider why the $O_2(a^1\Delta_g)$ loss frequency increases at pressures below 1.5 Torr. Quenching by ground-state O_2 will be negligible at these low pressures, and the ozone density will also be low (since it is produced by three-body recombination, it will represent a much lower fraction at 1.5 Torr than the 0.1% we estimate at 4 Torr) so this can also be neglected. Therefore, this effect must be caused by an increase in the $O_2(a^1\Delta_g)$ quenching probability at the borosilicate glass walls. The $O(^3P)$ atom surface loss probability (during discharge), γ_O, shows an analogous (but stronger) increase at low pressures (see below). This effect has been attributed to modification of the borosilicate glass surface by the increasing energy of ion bombardment at lower pressures [1]. We postulate that the observed increase of $\gamma_{O2(a)}$ at low pressures is also the result of energetic ion bombardment (during the discharge period preceding these afterglow measurements).

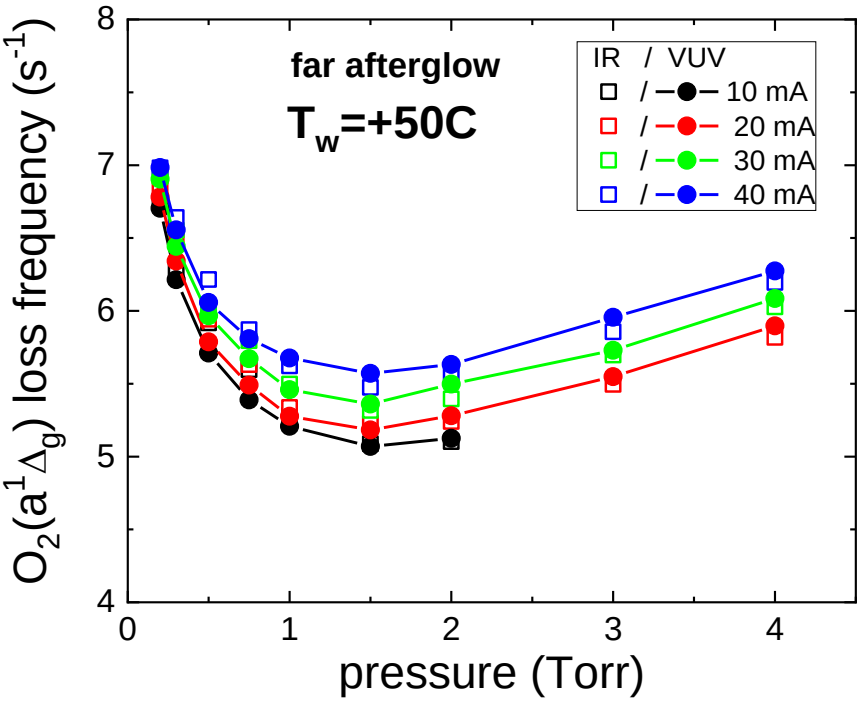

Figure 5. The $O_2(a^1\Delta_g)$ loss frequency in the late afterglow obtained from the IR emission decay as function of pressure for different currents. The $O_2(a^1\Delta_g)$ loss frequency determined from the rate of recovery of the $O_2(X^3\Sigma_g^-)$ density in the later afterglow (measured by VUV absorption) is also shown (see below).

3.2 $O_2(X^3\Sigma_g^-)$ kinetics

Examples of the $O_2(X^3\Sigma_g^-)$ VUV absorption during full modulation of the discharge for pressures of 1 Torr and 4 Torr are presented in Figures 6a and 6b. The decrease in the $O_2(X^3\Sigma_g^-)$ absorption when the discharge is ignited is caused by a combination of O_2 dissociation, excitation into metastable states (principally $O_2(a^1\Delta_g)$, as seen also from Figure 4) and gas heating/dilation. It is important to note here that the $O_2(X^3\Sigma_g^-)$ absorption cross-section increases with temperature at these photon energies [54,57], and the gas temperature is higher in the active discharge [1]. Therefore, it is not possible to determine the temporal behavior of the $O_2(X^3\Sigma_g^-)$ density through the whole modulation cycle directly from the VUV absorption, unless it is corrected for this change in absorption cross-section. This effect is most marked at higher O_2 pressures, both because the gas is hotter (since the dissipated power density increases with pressure at constant current density) and because at the lower photon energies used in this case, the cross-section increases more with the temperature. At the highest gas pressure and current used here (4 Torr 40 mA) the gas temperature reaches ~540 K [1]. Hudson [57] found that the cross-section at 7.117 eV increases

by about 25% between 300K and 600K, and by 42% at 7.085eV . Therefore, we estimate that the cross-section will decrease by about 20% as the gas cools from 540K (steady state discharge) to 323 K. At lower pressures and currents, the changes in the $O_2(X^3\Sigma_g^-)$ absorption cross-section are notably smaller.

We were not able to make time-resolved measurements of the gas temperature; however, simple thermal modelling (using the heat capacity and thermal conductivity of pure O_2) indicates that it will take at most 2-3 ms (at the highest pressure and current) for the gas to cool to the wall temperature. The kinetic measurements are fully consistent with this time-scale, which is very similar to that measured in fully-modulated CO_2 glow discharges in the same discharge tube by IR absorption [63]. After this initial cooling period the gas temperature will be in equilibrium with the tube wall at 323K and the $O_2(X^3\Sigma_g^-)$ absorption cross-section will be constant. Therefore, we only used the later afterglow data in our analysis.

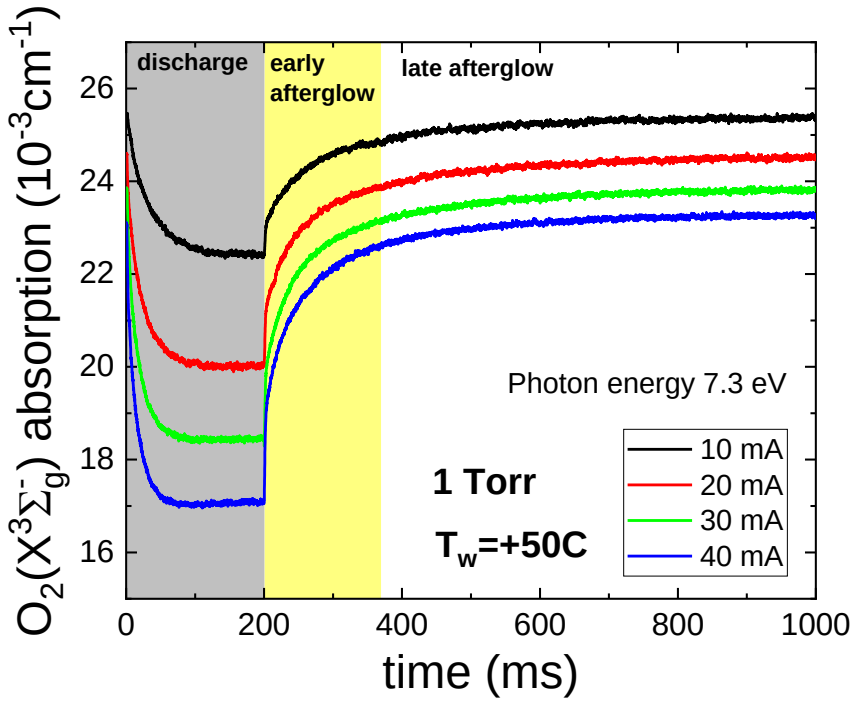

(a)

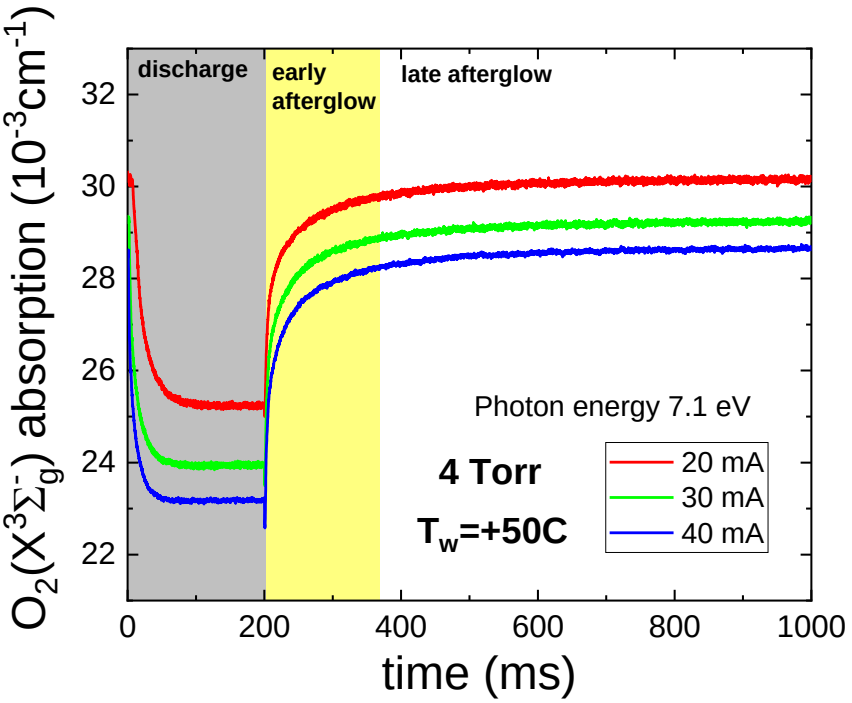

(b)

Figure 6. Dynamics of the $O_2(X^3\Sigma_g^-)$ absorption during full discharge modulation (discharge duration – 200 ms, afterglow duration – 800 ms). (a) 1 Torr and (b) 4 Torr.

After switching off the discharge the $O_2(X^3\Sigma_g^-)$ VUV absorption progressively recovers to its no-discharge value. Note here that the no-discharge gas density decreases with increasing discharge current: this is because the measurements are made in a sealed tube, with the gas

pressure (and thus the total number of O_2 molecules contained in the sealed tube) set when the discharge is on, i.e. when the gas is hotter and dissociated. The rate at which the $O_2(X^3\Sigma_g^-)$ VUV absorption recovers is complex due to the different processes occurring. In the first 2-3 ms the gas cools down to the wall temperature (T_w=323 K). During this short period the $O_2(X^3\Sigma_g^-)$ absorption cross-section decreases due to the temperature decrease. The data are not corrected for this effect, therefore the data with the discharge on, and in the immediate (first ≈4 ms) cooling period cannot be directly compared to the results from the later afterglow. As the gas at the tube axis cools and contracts, gas returns from the regions near the walls, causing the (on-axis) gas density to increase. These two effects, which occur on similar timescales, tend to cancel each other out. Overall, for example at 4 Torr and 40 mA, an initial fast dip of about 2.5% in the absorption is observed, followed by a slightly lower rise. At lower pressures and currents the effects due to temperature changes are concomitantly smaller, and in all cases do not last longer than 4 ms. A further effect contributing to the $O_2(X^3\Sigma_g^-)$ density increase in this initial phase is the fast quenching of $O_2(b^1\Sigma_g^+)$. However, from absolute optical emission and Fourier-transform Vacuum Ultraviolet absorption measurements [49] we estimate that molecules in this state only represent a maximum of 0.5% of the gas composition, and can be neglected.

After the initial gas temperature stabilization period, the $O_2(X^3\Sigma_g^-)$ density (which can now be deduced accurately from the VUV absorption) recovers more slowly. However, this recovery is not described by a single exponential rate (i.e. function of the type (A-B·exp(-kt)), but is faster in the beginning, slowing down at later times.

In order to see this behavior more clearly, let us consider the time-resolved *depletion* of the $O_2(X^3\Sigma_g^-)$ density, defined as $\delta[O_2(X^3\Sigma_g^-)](t) = [O_2(X^3\Sigma_g^-)]_0 - [O_2(X^3\Sigma_g^-)](t)$. Here $[O_2(X^3\Sigma_g^-)]_0$ is the no-discharge density of O_2, and $[O_2(X^3\Sigma_g^-)](t)$ is the $O_2(X^3\Sigma_g^-)$ density observed during the pulsing cycle. Ignoring the first few ms, $[O_2(X^3\Sigma_g^-)](t)$ can be calculated using the absorption cross-section for O_2 at T=323 K. Figures 7a and 7b show $\delta[O_2(X^3\Sigma_g^-)](t)$ on a log scale (black points) at 1 Torr, 10mA and 4 Torr, 40 mA, respectively. The $O_2(a^1\Delta_g)$ density measured by IR emission is also shown (red points), scaled to fit the $O_2(X^3\Sigma_g^-)$ depletion curve in the late afterglow (150 ms after discharge interruption, i.e. time = 350ms in figure 7). It can be seen that in the later afterglow the rate of recovery of $O_2(X^3\Sigma_g^-)$ corresponds exactly to the decay of the $O_2(a^1\Delta_g)$ density. The dashed green lines in Figures 7a and 7b show single-exponential fits to the VUV data in the late afterglow (t > 350 ms, with rates of $5.28s^{-1}$ at 1 Torr, 10 mA and $6.27s^{-1}$ at 4 Torr 40 mA), extrapolated back to the beginning of the afterglow. The single exponential decay of the $O_2(a^1\Delta_g)$ density in the late afterglow indicates a constant surface loss probability of $O_2(a^1\Delta_g)$. The (later afterglow) $O_2(X^3\Sigma_g^-)$ recovery rates deduced from these exponential fits were shown above

in Figure 5, alongside the $O_2(a^1\Delta_g)$ loss frequencies measured by IR emission. The $O_2(X^3\Sigma_g^-)$ recovery rates agree almost perfectly with the $O_2(a^1\Delta_g)$ loss frequencies. Thus, in this late afterglow period (after the $O(^3P)$ atoms are gone), quenching of $O_2(a^1\Delta_g)$ to $O_2(X^3\Sigma_g^-)$ on the borosilicate tube surface is the only process leading to $O_2(X^3\Sigma_g^-)$ recovery.

Furthermore, since we accurately know the density of $O_2(X^3\Sigma_g^-)$ (the VUV absorption cross-section is calibrated against the gas pressure and temperature, without discharge), the density of $O_2(a^1\Delta_g)$ is also known accurately, since these two molecules are the only components remaining in the late afterglow. This therefore allows absolute calibration of the IR emission measurements. This scaling of the $O_2(a^1\Delta_g)$ IR emission measurements was used in the following analysis. It should be noted that the $O_2(a^1\Delta_g)$ densities obtained using the two IR calibration techniques described above fall to either side of the values determined from the $O_2(X^3\Sigma_g^-)$ recovery.

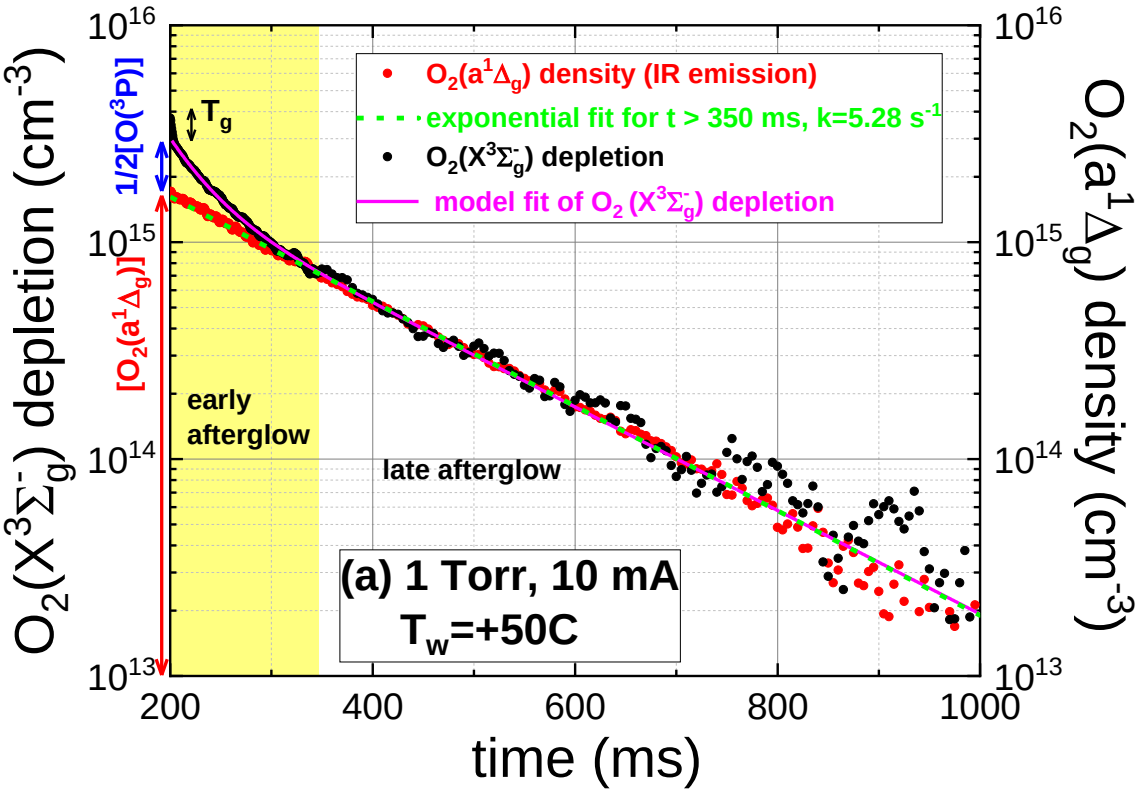
$O_2(a^1\Delta_g)$ density (IR emission)
exponential fit for t > 350 ms, k=5.28 s^{-1}
$O_2(X^3\Sigma_g^-)$ depletion
model fit of $O_2(X^3\Sigma_g^-)$ depletion
T_g
1/2[$O(^3P)$]
[$O_2(a^1\Delta_g)$]
early afterglow
late afterglow
(a) 1 Torr, 10 mA
T_w=+50C
$O_2(X^3\Sigma_g^-)$ depletion (cm^{-3})
$O_2(a^1\Delta_g)$ density (cm^{-3})
time (ms)

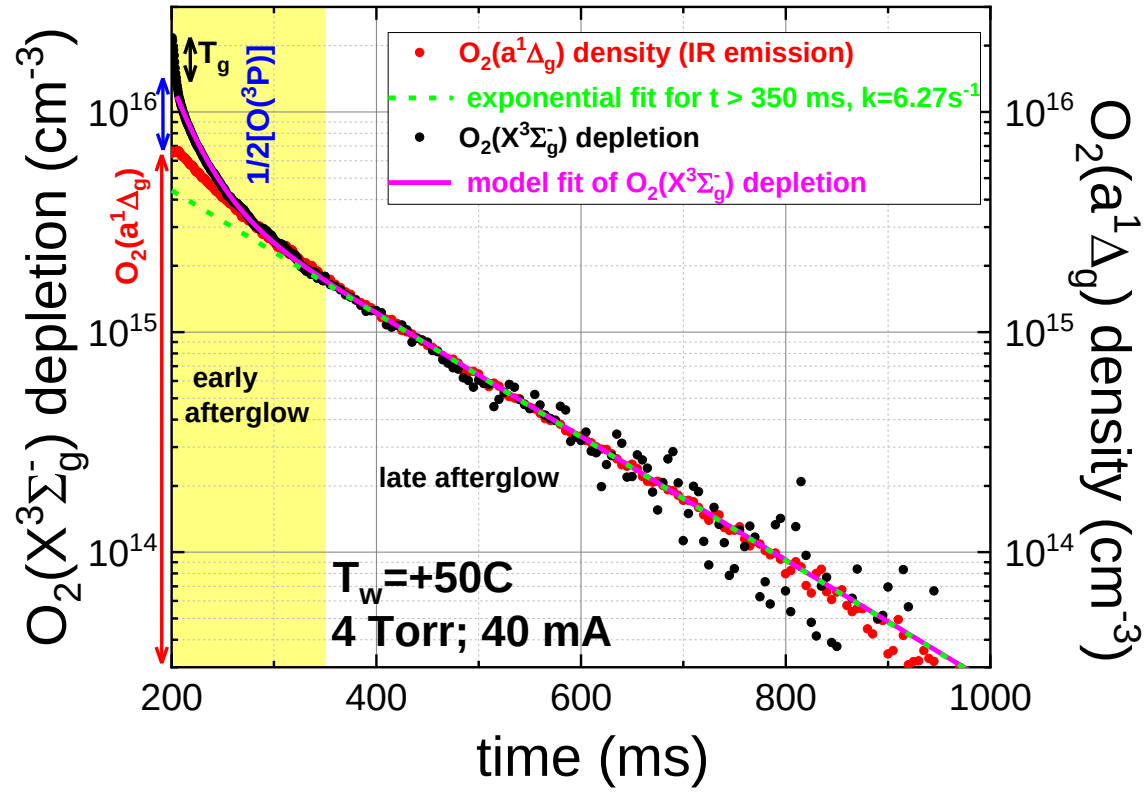
$O_2(a^1\Delta_g)$ density (IR emission)
exponential fit for t > 350 ms, k=6.27s^{-1}
$O_2(X^3\Sigma_g^-)$ depletion
model fit of $O_2(X^3\Sigma_g^-)$ depletion
T_g
1/2[$O(^3P)$]
$O_2(a^1\Delta_g)$
early afterglow
late afterglow
T_w=+50C
4 Torr; 40 mA
$O_2(X^3\Sigma_g^-)$ depletion (cm^{-3})
$O_2(a^1\Delta_g)$ density (cm^{-3})
time (ms)

(a) (b)

Figure 7. Examples of dynamics of the $O_2(X^3\Sigma_g^-)$ depletion, $\delta[O_2(X^3\Sigma_g^-)](t)$, (black points) and the $O_2(a^1\Delta_g)$ density (IR emission data: red points) in the afterglow of a fully-modulated discharge (discharge duration – 200 ms, afterglow duration – 800 ms). (a) – 1 Torr, 10 mA and (b) – 4 Torr, 40 mA. The green dashed line is a single-exponential fit to the $O_2(X^3\Sigma_g^-)$ depletion in the late afterglow. The magenta curve is a fitted model of the $O_2(X^3\Sigma_g^-)$ depletion in the discharge afterglow, allowing for the contributions from $O_2(a^1\Delta_g)$ quenching by the different mechanisms and $O(^3P)$ atom recombination (see text). The amplitudes of the $O(^3P)$ atom recombination and $O_2(a^1\Delta_g)$ quenching components, extrapolated back to the steady-state discharge, are shown in blue and red respectively on the left axes.

3.3 Early afterglow : O (^{3}P) kinetics

Now let us examine the processes occurring in the early afterglow (in the period after the gas cooling period up to ~100 ms). In this period, both the $O_2(X^3\Sigma_g^-)$ recovery and $O_2(a^1\Delta_g)$ decay dynamics are significantly faster than in the late afterglow. As shown by Booth et al. [1] in a similar discharge tube, the $O(^3P)$ atom density represents a significant fraction of the gas composition in the steady-state discharge, with a loss frequency (in the active discharge) varying from 10 to 70s^{-1} depending on the pressure and current. The dominant O atom loss process is surface-catalyzed recombination into O_2. However, the O atom loss frequencies in specific discharge tubes has been found to vary depending on the history of the tube, therefore we measured the (active discharge) loss frequency in the tube used here by time-resolved actinometry during partial discharge current modulation [1,9]. The $O(^3P)$ loss frequency, ν_q^O, during the discharge (obtained from the exponential fits) is presented as a function of pressure for different currents in Figure 8. The trends with pressure and current are similar to those presented in Booth et al. [1], but the rates are higher, particularly at low pressure, indicating a higher surface catalytic activity (a higher surface density of absorption sites or surface defects) for the particular tube used in these measurements. The $O(^3P)$ loss frequency increases sharply with decreasing pressure below 1 Torr. Booth et al. [1] postulated such an increase is the consequence of energetic ion bombardment at low pressure.

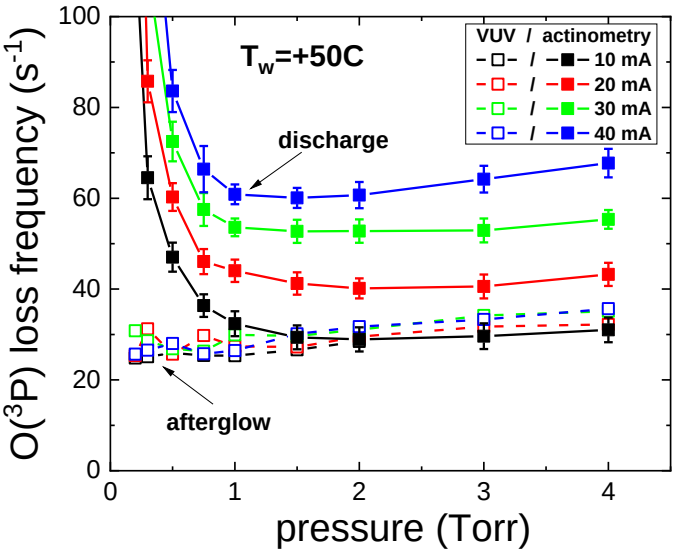

Figure 8. $O(^3P)$ atom loss frequency ν_q^O in the early afterglow (open symbols; ν_q^O obtained from $O_2(X^3\Sigma_g^-)$ recovery dynamics) and in the active discharge (solid symbols; ν_q^O obtained by time-resolved actinometry) as function of pressure for different currents.

If the surface loss probabilities for $O_2(a^1\Delta_g)$ and $O(^3P)$ are constant in the afterglow, the $O_2(X^3\Sigma_g^-)$ recovery dynamics (after gas temperature relaxation) should be represented by a bi-exponential decay. Figure 7 shows that this model indeed fits the experimental data at 1 Torr, 10 mA, allowing the oxygen atom loss rate to be determined. However, as noted above, at higher pressures there is additional quenching of $O_2(a^1\Delta_g)$ by $O(^3P)$ atoms, causing the $O_2(a^1\Delta_g)$ decay rate to be somewhat faster in the early afterglow compared to the single exponential rate observed in the late afterglow (green dashed line in Figure 7). Fortunately, the IR emission measurements (shown in figure 4) give the true temporal behavior of the $O_2(a^1\Delta_g)$ density decay (red symbols in Fig. 7, scaled to the VUV measurements), allowing us to separate the contributions of $O(^3P)$ recombination and $O_2(a^1\Delta_g)$ quenching to the $O_2(X^3\Sigma_g^-)$ recovery. The time-resolved oxygen atom density was determined from the $O_2(X^3\Sigma_g^-)$ recovery after subtracting the corresponding scaled $O_2(a^1\Delta_g)$ density curve, multiplied by two (since two atoms make one molecule). This was then fitted to an exponential decay.

The $O(^3P)$ loss frequency in the early afterglow (determined from the initial $O_2(X^3\Sigma_g^-)$ recovery, with the contribution from $O_2(a^1\Delta_g)$ subtracted) is shown in Figure 8 by open symbols. In contrast to the measurements made during the discharge, the afterglow $O(^3P)$ loss frequency changes little with the discharge current, and only increases slightly with pressure. Only for pressures above 1 Torr and at the lowest current (10 mA) is this comparable to the loss rates in the

active discharge (measured by actinometry). Notably, the increase of the loss rate at low pressures is absent. Furthermore, the increase in loss rate with discharge current observed in the *active* discharge (caused by the higher gas temperature [1]) is not seen in the afterglow values. The loss rate corresponds to an $O(^3P)$ atom surface loss probability of $\gamma_O \approx 1.1 \cdot 10^{-3}$. This value is somewhat higher than the minimal value determined by Booth et al. [1] ($\gamma_O \approx 0.8 \cdot 10^{-3}$) at 1 Torr 10 mA, but in a different discharge tube. The small increase with pressure of the $O(^3P)$ afterglow loss rate (corresponding to an increase with pressure of ~2.5±0.5 s^{-1}/Torr) can be attributed to three-body recombination of oxygen atoms in the volume, notably:

1) $O(^3P) + O_2 + O_2 \rightarrow O_3 + O_2$ $k_{O3}=6.2 \cdot 10^{-34}(300/T)^2$ cm^6/s [64],

giving a loss rate of ~7 s^{-1} at 4 Torr, accounting for most of the trend. There is also the possibility of some production of ozone at the tube surface, the rate of which has been observed to increase with pressure :

2) $O(^3P) + O_2 + wall \rightarrow O_3 + wall$ ($\gamma_{O3} \approx (10^{-5}–10^{-4}) \cdot P_{O2}$[Torr] [62,53,65]

The small amount of ozone produced by these two processes is coherent with our estimate of a maximal ozone concentration of $1.5 \cdot 10^{14}$ at 4 Torr/40 mA, estimated above from the $O_2(a^1\Delta_g)$ loss increase in the later afterglow. This represents only 0.1% of the total gas composition, which is insignificant compared to the densities of $O(^3P) + O_2(a^1\Delta_g)$. It is important to note here that the ozone concentration during the active discharge period will be considerably lower than in the afterglow, since in the active discharge it is destroyed efficiently both by electron impact and by thermal decomposition at higher gas temperatures [1]. In the afterglow, ozone can further react with $O(^3P)$:

3) $O(^3P) + O_3 \rightarrow 2O_2$ $k_r=8 \cdot 10^{-12}$ exp(-2060/T) cm^3 $molecule^{-1}$ s^{-1} cm^6/s [66]

Finally, a small additional loss of $O(^3P)$ may occur by three-body recombination into molecular oxygen:

4) $O(^3P) + O(^3P) + O_2 \rightarrow O_2 + O_2$ $k_r=3.8 \cdot 10^{-30}/T \cdot \exp(-170/T)$ cm^6/s [60]

3.4 Composition of the steady state discharge

The amplitudes of the two components of the $O_2(X^3\Sigma_g^-)$ recovery, due to $O_2(a^1\Delta_g)$ quenching and O atom recombination, indicate the mole-fractions of these two species in the steady-state discharge. Indeed, these can be deduced from the relative amplitudes of the components of the PMT signal, with no need to calculate the actual $O_2(X^3\Sigma_g^-)$ density using the absorption cross-section. Combined with knowledge of the absolute $O_2(X^3\Sigma_g^-)$ density (simply from the gas pressure and temperature without discharge), the absolute densities of all three species in the discharge can be determined. However, first it is necessary to determine whether it is valid to extrapolate back

to the moment when the discharge is stopped, through the immediate post-discharge period, when fast gas cooling occurs. The loss frequencies of both transient species will be somewhat higher in this period. This effect is most significant at the highest pressures and currents, where the gas temperature is highest, and the cooling is longest (due to the higher total heat capacity of the gas). We are not able to follow the O atom dynamics directly in this period (when the $O_2(X^3\Sigma_g^-)$ absorption cross-section is changing). However, even at 4 Torr/40 mA the $O_2(X^3\Sigma_g^-)$ recovery curve (Figure 7(b)) the gas cooling period only lasts for ≈3 ms. This is short compared to the loss frequency of $O(^3P)$ atoms ($68s^{-1}$ in the active discharge, dropping to $36s^{-1}$ in the afterglow). We estimate that this effect could lead to a maximal underestimation of the O atom density of 10% in this worst case. At the lowest gas pressures and highest current there is an even bigger change in the $O(^3P)$ loss frequency between the active discharge and the afterglow. In this case, the change in the surface reactivity is not caused by a change in the gas temperature (which is negligible in this case) but appears to be linked to ion bombardment of the surface during the active discharge, which stops immediately when the discharge is stopped. For simplicity, we have assumed that the surface recombination probability also changes immediately. At these low pressures the $O_2(X^3\Sigma_g^-)$ measurement is not significantly perturbed by the temperature-dependent absorption cross-section, so the observed VUV absorption accurately reflects the $O_2(X^3\Sigma_g^-)$ density. A small, fast jump in the $O_2(X^3\Sigma_g^-)$ density is observed in the first few milliseconds of the afterglow, which can be entirely explained by the return of gas from near the tube walls to the axis (where the measurements are made) as the gas temperature profile relaxes to uniform equilibrium with the wall temperature. After this the data can be well fitted with the bi-exponential function, using two rate constants representing the decay rates of oxygen atoms and of $O_2(a^1\Delta_g)$. There is no evidence significantly faster oxygen atom decay in the initial afterglow. Therefore, we conclude that extrapolation of the oxygen atom mole-fraction to the beginning of the afterglow is valid. We plan to further investigate the rapid change in surface reactivity when the discharge is stopped using direct measurements of the oxygen atom density, but this is not the subject of this paper.

In the case of $O_2(a^1\Delta_g)$, the dynamics are measured directly from the IR emission. As shown in Figure 4, there is only a small change when the discharge current is stopped, which can be attributed to gas movement from the walls towards the axis (and possibly some perturbation of the IR detector some electromagnetic noise from the high-voltage switching).

The amplitudes (extrapolated back to the beginning of the afterglow) of the $O(^3P)$ recombination and $O_2(a^1\Delta_g)$ quenching contributions to the $O_2(X^3\Sigma_g^-)$ recovery are indicated (in red and blue respectively) on the left axes of Figure 7. The total gas density, N (= $[O_2(X^3\Sigma_g^-)]$

+[O]+ [$O_2(a^1\Delta_g)$]), is known from the asymptotic level of the $O_2(X^3\Sigma_g^-)$ absorption in the late afterglow (see Figure 6).

First we will consider the density of the metastable $O_2(a^1\Delta_g)$ state. The $[O_2(a^1\Delta_g)]/N$ mole fraction at the beginning of afterglow was obtained from the $O_2(a^1\Delta_g)$ IR emission, scaled to the $O_2(X^3\Sigma_g^-)$ recovery plot in the late afterglow (as shown in Figure 6). This ratio, as well as the ratio $[O_2(a^1\Delta_g)]/[O_2(X^3\Sigma_g^-)]$, is shown as a function of pressure for different currents in Figures 9a and 9b respectively. Both values pass through a small maximum with pressure (around 0.75-1 Torr) before decreasing slowly. They also both increase monotonically with current, but less than linearly. This implies that the principal creation mechanism for $O_2(a^1\Delta_g)$ is electron-impact excitation from the ground state. The discharge current (and therefore the electron density) stabilizes very quickly after discharge ignition (although it may show some slower drifts due to slower changes of the chemical composition of the gas). Therefore the timescale of the $O_2(a^1\Delta_g)$ equilibration after ignition is determined by its loss processes. As Figure 4 shows, the $O_2(a^1\Delta_g)$ density reaches steady state after discharge ignition in a time much shorter than the $O_2(a^1\Delta_g)$ lifetime in the afterglow. This indicates that there are additional fast $O_2(a^1\Delta_g)$ loss processes in the active discharge. These can be attributed principally to electron-impact processes: both super-elastic scattering (back to the ground state) and excitation, mainly to the $b^1\Sigma_g^+$ state. It is also possible that the rate of $O_2(a^1\Delta_g)$ quenching by O atoms increases with gas temperature. Figure 4 further shows that the $O_2(a^1\Delta_g)$ density equilibrates faster at higher currents, showing the dominant role of electron impact processes in both the creation and destruction of $O_2(a^1\Delta_g)$ in the active discharge.

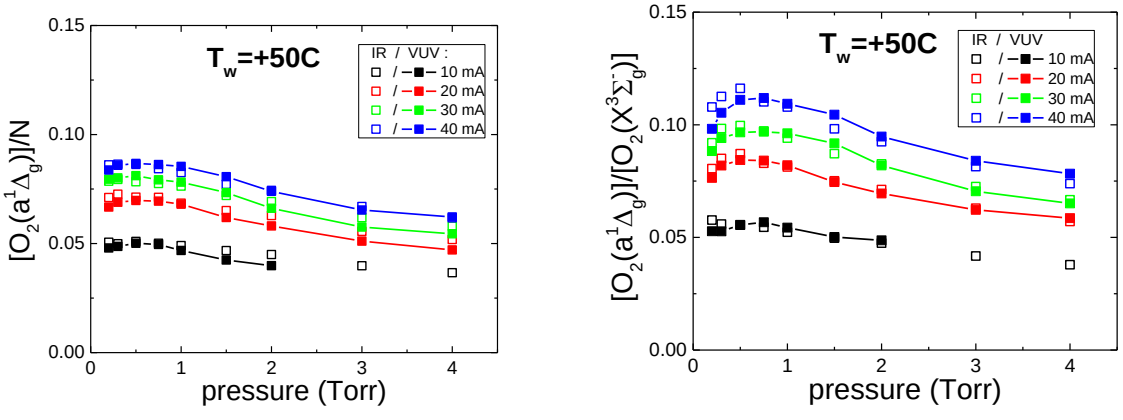

(a) (b)

Figure 9. (a) $[O_2(a^1\Delta_g)]/N$ mole fraction and (b) $[O_2(a^1\Delta_g)]/[O_2(X^3\Sigma_g^-)]$ ratio in discharge as function of pressure for different currents. The solid squares are data from VUV absorption measurements, the open squares are from IR emission.

The oxygen atom mole-fraction, $[O(^3P)]/N$, could be then determined after subtracting the $[O_2(a^1\Delta_g)](t)$ curve from $\delta[O_2(X^3\Sigma_g^-)](t)$, and fitting the remaining curve with a single-exponential decay. The $O(^3P)$ atom mole-fraction in the active discharge is equal to twice this amplitude (since two atoms are needed to make one molecule). The $O(^3P)$ mole fraction obtained in this way, $[O(^3P)]/N$, is shown as a function of pressure and current in Figure 10a.. It passes through a maximum at 1 Torr, which corresponds to the minimum of the loss frequency (see Figures 8 and 10). Figure 10b shows the ratio of the $O(^3P)$ density to the ground state $O_2(X^3\Sigma_g^-)$ density.

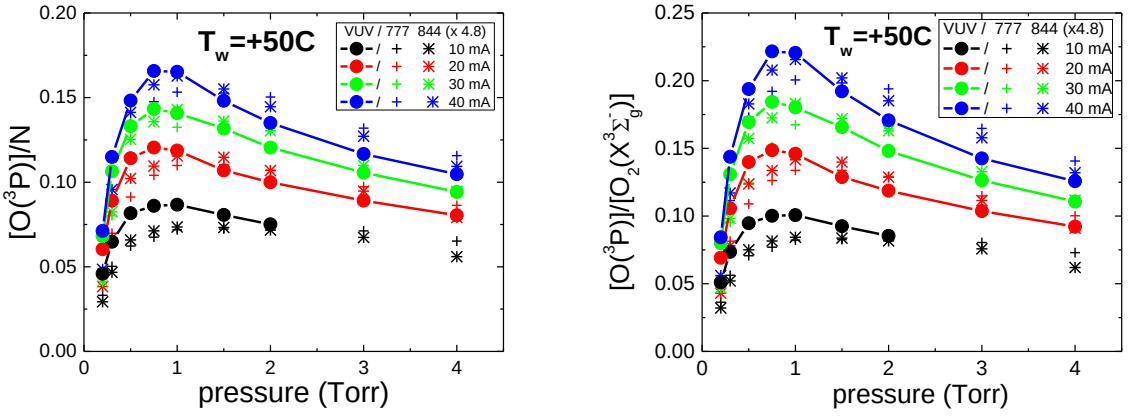

(a) (b)

Figure 10. (a) $[O(^3P)]/N$ mole fraction and (b) $[O(^3P)]/[O_2(X^3\Sigma_g^-)]$ ratio in the active discharge as a function of pressure for different currents. The solid squares are obtained from the VUV absorption measurements. The crosses present thee results of actinometry for the 777 nm and 844 nm lines of O atoms, multiplied by a factor of 4.8.

The oxygen atom mole fraction $[O(^3P)]/N$ was also determined by optical emission actinometry (crosses in Figure 10). In order to obtain these values from the O/Ar line emission intensity ratios, it is necessary to calculate an actinometry coefficient, as described in Booth et al. [1]. However, such calculations require excitation cross-sections. In the case of oxygen and argon (and generally for atoms) there are only a few measurements, and even fewer theoretical calculations of these cross-sections, and the different data are in rather poor agreement, especially in the crucial near-threshold energy region. In the current work (and in contrast to [1]) we chose to use cross sections from recent, widely-acclaimed ab-initio calculations: Tayal and Zatsarinny for oxygen atoms [22] and Zatsarinny et al. for argon [58]. The actinometry results obtained follow the relative trends in oxygen atom mole fraction reasonably well, but it was necessary to increase the actinometry results by a factor of 4.8 (as shown in Figure 10) in order to obtain the same absolute values. Excitation via collisional cascades from higher states, or (in the case of argon)

stepwise excitation via metastables, are unlikely to make significant contributions at these low values of the reduced electric field. Comparable agreement of the oxygen mole-fraction values obtained by actinometry to our VUV measurements can be achieved using different sets of excitation cross sections, for example those used in [10] or [17-19], but with a different correction factor. For example, using the cross sections used in Booth et al. [1] requires a correction factor ~1.5-2.

3.5 Kinetic Model

In order to better understand the dynamics of $O(^3P)$, $O_2(a^1\Delta_g)$ and $O_2(X^3\Sigma_g^-)$ in the afterglow we created a kinetic model. The model only included these three species; higher excited states of O_2, notably $O_2(b^1\Sigma_g^+)$, were not included due to their low density and fast quenching in the early afterglow. The experimentally-obtained mole-fractions of the $O(^3P)$, $O_2(a^1\Delta_g)$ and $O_2(X^3\Sigma_g^-)$ in the discharge were used as the initial values. The calculations were performed either at constant pressure or at constant volume. The list of the reactions included is presented in Table 1.

Table. 1 Processes included in the simulation of the $O_2(X^3\Sigma_g^-)$ recovery kinetics in the discharge afterglow.

Process	Rate constant [a,b]	Reference
Major processes in the studied conditions		
$O(^3P) + O_{wall} \rightarrow O_2(X^3\Sigma_g^-)$ + wall	$8\cdot10^{-4}$	this work
$O_2(a^1\Delta_g)$ + wall $\rightarrow O_2(X^3\Sigma_g^-)$ + wall	$2.2\cdot10^{-4}$	this work
$O_2(a^1\Delta_g) + O(^3P) \rightarrow O_2(X^3\Sigma_g^-) + O(^3P)$	$7.6\cdot10^{-16}$	[59]
Minor processes in the studied conditions		
$O(^3P) + O(^3P) + O_2 \rightarrow O_2(X^3\Sigma_g^-) + O_2$	$3.34\cdot10^{-30}/T\cdot\exp(-170/T)$	[60]
$O(^3P) + O(^3P) + O_2 \rightarrow O_2(a^1\Delta_g) + O_2$	$0.39\cdot10^{-30}/T\cdot\exp(-170/T)$	[67,68]
$O(^3P) + O(^3P) + O_2 \rightarrow O_2(b^1\Sigma_g^+) + O_2$	$0.07\cdot10^{-30}/T\cdot\exp(-170/T)$	[67,68]
$O(^3P) + O(^3P) + O_2 \rightarrow O_3 + O(^3P)$	$2.15\cdot10^{-34}\cdot\exp(345/T)$	[64]
$O(^3P) + O_2(X^3\Sigma_g^-) + O_2 \rightarrow O_3 + O_2$	$6.2\cdot10^{-34}(300/T)^2$	[64]
$O_2(a^1\Delta_g) + O_2 \rightarrow O_2(X^3\Sigma_g^-) + O_2$	$2.2\cdot10^{-18}(T/300)^{0.8}$	[60]
$O_2(a^1\Delta_g) + O_3 \rightarrow O_2(X^3\Sigma_g^-) + O(^3P) + O_2(X^3\Sigma_g^-)$	$5.1\cdot10^{-11}\cdot\exp(-2840/T)$	[61]
$O_2(a^1\Delta_g) + O_2(a^1\Delta_g) \rightarrow O_2(X^3\Sigma_g^-) + O_2(b^1\Sigma_g^+)$	$7\cdot10^{-28}/T^{3.8}\cdot\exp(700/T)$	[69]
$O(^3P) + O_3 \rightarrow O_2 + O_2$	$8\cdot10^{-12}\cdot\exp(-2080/T)$	[66]

[a] Rate constants of binary reactions are given in cm^3/s. For three body reactions, in cm^6/s.

[b] For surface loss, the corresponding loss probabilities are presented.

The simulated dynamics of the $O(^3P)$, $O_2(a^1\Delta_g)$ and $O_2(X^3\Sigma_g^-)$ mole fractions in the afterglow at 1 Torr, 10 mA and at 4 Torr, 40 mA are presented in Figures 11a and 11b respectively. The experimental data are also shown. The model quite adequately reproduces decays of $O(^3P)$ and $O_2(a^1\Delta_g)$, and the corresponding $O_2(X^3\Sigma_g^-)$ recovery. In fact, the $O_2(X^3\Sigma_g^-)$ dynamics is determined almost entirely by the three processes: i) $O(^3P)$ surface recombination, ii) $O_2(a^1\Delta_g)$ quenching at the walls and iii) $O_2(a^1\Delta_g)$ quenching by O atoms. This indicates that the O_3 and O_2 $(b^1\Sigma_g^+)$ densities are low can be neglected. It should be also noted that the excellent agreement between the calculated and experimental data is a consequence of using the experimentally-determined $O(^3P)$ and $O_2(a^1\Delta_g)$ surface loss probabilities.

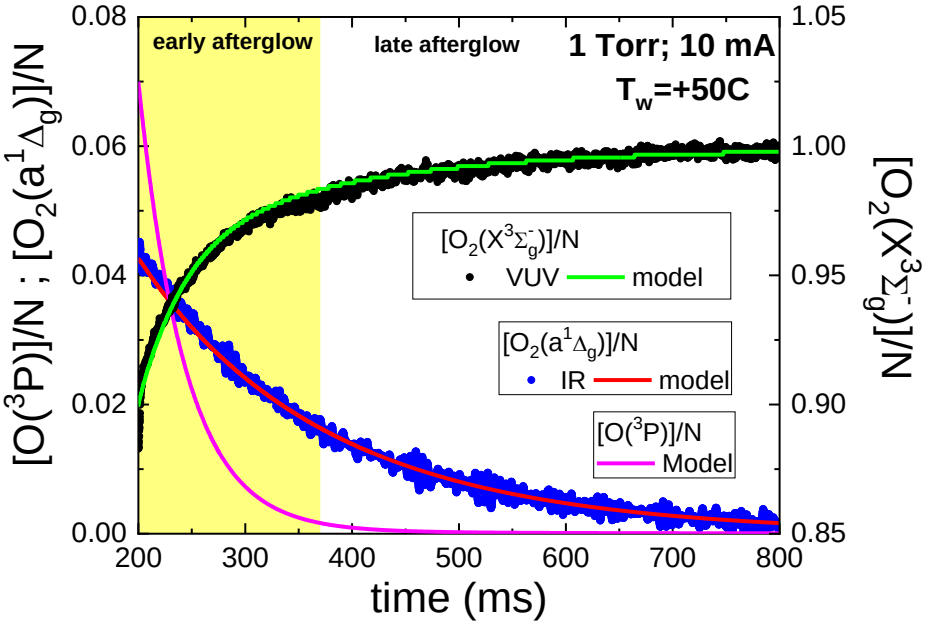

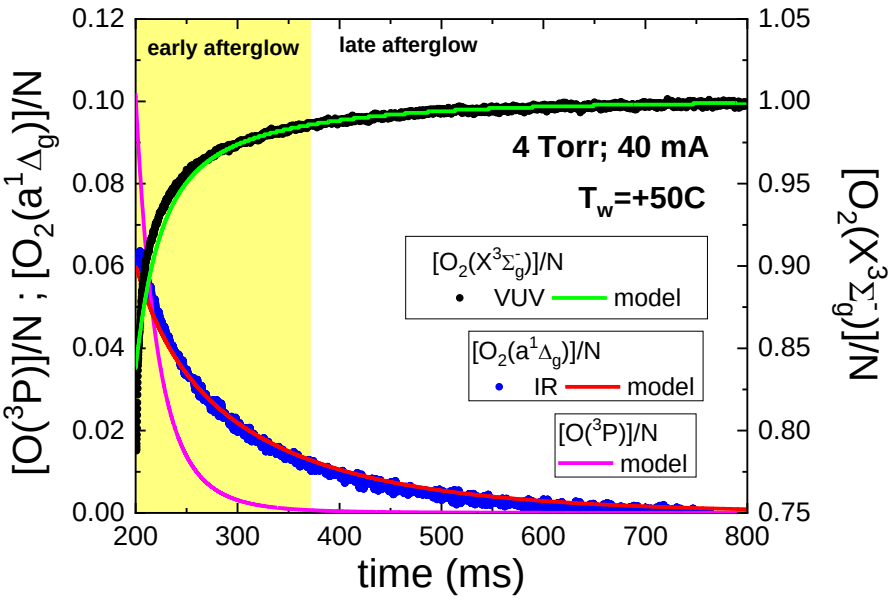

(a) (b)

Figure 11. Dynamics of $[O(^3P)]/N$, $[O_2(a^1\Delta_g)]/N$ and $[O_2(X^3\Sigma_g^-)]/N$ mole fractions in the discharge afterglow for 1 Torr, 10 mA (a) and 4 Torr, 40 mA (b). Solid lines are from the model. Points are experimental data.

4. Conclusion

We have presented a method that allows the measurement of the absolute densities of $O(^3P)$ atoms and $O_2(a^1\Delta_g)$ molecules in a pure O_2 discharge without any a priori calibration procedure or knowledge of transition strengths (an ab initio method). It is based on observation of the recovery dynamics of the undissociated ground-state molecule, $O_2(X^3\Sigma_g^-)$, after extinction of the discharge. The temporal behavior of the $O_2(X^3\Sigma_g^-)$ number density was measured by VUV absorption spectroscopy, using the monochromatic branch of the DESIRS beamline at synchrotron SOLEIL, although the same methodology could be used with a different density measurement method. The method was validated in O_2 glow dc discharges at pressures in the range of 0.2-4 Torr.

In parallel, the $O_2(a^1\Delta_g)$ dynamics was measured by IR emission spectroscopy, and the oxygen atom mole fraction $[O(^3P)]/N$ during the active discharge was determined by the Ar actinometry method. The $O(^3P)$ loss frequency in the active discharge was determined by time-resolved actinometry in partially modulated discharges. When the discharge is ignited, the $O_2(X^3\Sigma_g^-)$ density drops due to gas heating, dissociation and excitation into metastable states. After switching off the discharge, the initial $O_2(X^3\Sigma_g^-)$ density recovers progressively. In the first few milliseconds, the $O_2(X^3\Sigma_g^-)$ density shows a small fast jump up due to gas cooling and convection. Subsequently, a slower $O_2(X^3\Sigma_g^-)$ density recovery is observed due to $O(^3P)$ recombination and, at even longer

times, $O_2(a^1\Delta_g)$ quenching. The time-scales of $O_2(a^1\Delta_g)$ quenching and $O(^3P)$ recombination differ by almost an order of magnitude, since the losses of both occur principally at the tube walls, with the surface loss probability for $O(^3P)$ almost an order of magnitude higher than for $O_2(a^1\Delta_g)$. This allows separation of the $O(^3P)$ and $O_2(a^1\Delta_g)$ contributions to the $O_2(X^3\Sigma_g^-)$ density recovery dynamics, as well as determination of the mole fractions $[O(^3P)]/N$ and $[O_2(a^1\Delta_g)]/N$ at the end of the discharge.

This method could be applied to other discharges in pure O_2, provided that the discharge is contained (so that total mass density of the system is conserved), that there is adequate spatially uniform across the probed volume, that the characteristic lifetimes of the transitory species involved (electrons, $O(^3P)$ and $O_2(a^1\Delta_g)$ in this case) are sufficiently different, and that other species (O_3, $O_2(b^1\Sigma_g^+)$) have negligible densities. One could also imagine applying the same strategy to discharges in other pure diatomic gases, if analogous conditions are met (principally that the ground state density can be measured, and that the number of transitory species present in the discharge is small and their kinetics can be separated). It is unlikely to be applicable atmospheric pressure discharges due to their significant spatial gradients and the fact that they are often not contained systems. Furthermore, this approach can also be useful for the accurate absolute calibration or validation of other techniques such as for example, TALIF and actinometry, which can then be applied in more challenging experimental conditions.

Analysis of the dynamics of the $O_2(X^3\Sigma_g^-)$ and $O_2(a^1\Delta_g)$ densities in the afterglow by a kinetic model confirms the correctness of this approach. It was shown that the $O_2(a^1\Delta_g)$ IR emission decay agrees very well with the $O_2(X^3\Sigma_g^-)$ recovery dynamics in the late afterglow, and corresponds to an $O_2(a^1\Delta_g)$ surface loss with a probability $\sim 2.2\cdot10^{-4}$. An additional $O_2(a^1\Delta_g)$ loss process is observed in the early afterglow, and can be attributed to quenching by $O(^3P)$. While the IR emission measurements aided in the analysis, the contribution of this mechanism to the $O_2(X^3\Sigma_g^-)$ recovery could also be calculated, since the rate constant is known with sufficient accuracy, so that VUV absorption measurements alone could be used to deduce the kinetics and densities of the two species. The $O(^3P)$ loss in the afterglow is mainly caused by surface atom recombination, with a probability of $\sim 1.1\cdot10^{-3}$, estimated from the $O_2(X^3\Sigma_g^-)$ density recovery dynamics in the early afterglow. This only agrees well for the lowest current and above 1 Torr with the value obtained by time-resolved actinometry in the active discharge.

These results also provide the absolute $O(^3P)$ and $O_2(a^1\Delta_g)$ mole fractions in the discharge. We find that the actinometry technique follows the trends in the $O(^3P)$ density very well, but appears to systematically underestimate the absolute mole-fraction by a factor that can be as high

as 5, depending on the excitation cross-sections used. This suggests that the excitation cross sections for oxygen atoms, widely used for actinometry, are underestimated.

Acknowledgements

This research was conducted in the scope of the KaPPA International Associated Laboratory (LIA), performed within the LABEX Plas@par project, and received financial state aid managed by the Agence Nationale de la Recherche, as part of the programme "Investissements d'avenir" under the reference ANR-11-IDEX-0004-02. The Russian team is grateful to the Russian Foundation of Basic Research (RFBR) for supporting this work (grant 16-52-16024). A.C. is grateful to the Labex Plas@Par and to Synchrotron SOLEIL for a co-supervised PhD grant. We are grateful to Synchrotron SOLEIL for providing beamtime under the projects numbered 20170465 and 20180690.

References

[1] Booth J P, Guaitella O, Chatterjee A, Drag C, Guerra V, Lopaev D, Zyryanov S, Rakhimova T, Voloshin D and Mankelevich Yu 2019 *Plasma Sources Sci. Technol.* **28** 055005
[2] Vašina P, Kudrle V, Tálský A, Botŏs ., Mrázková M and Měsko M 2004 *Plasma Sources Sci. Technol.* **13** 668
[3] Herron J T, Franklin J L, Bradt P and Dibeler V H 1959 *J. Chem. Phys.* **30** 879
[4] Ricard A, Moisan M and Moreau S 2001 *J. Phys. D: Appl. Phys.* **34** 1203
[5] Tserepi A D and Miller T A 1995 *J. Appl. Phys.* **77** 505
[6] Rakhimova T V, Palov A P, Mankelevich Yu A, Popov N A and Carroll D L 2007 *Proceedings of SPIE* **6346** 634622-1
[7] Singh H, Coburn J W and Graves D B 2000 *J. Vac. Sci. & Technol.* A **18** 299
[8] Macko P, Veis P and Cernogora G 2004 *Plasma Sources Sci. Technol.* **13** 251
[9] Lopaev D V and Smirnov A V 2004 *Plasma Physics Reports* **30** 882
[10] Pagnon D, Amorim J, Nahorny J, Touzeau M and Vialle M 1995 *J. Phys. D: Appl. Phys.* **28** 1856
[11] Bousquet A, Cartry G and Granier A 2007 *Plasma Sources Sci. Technol.* **16** 597
[12] Kristof J, Macko P and Veis P 2012 *Vacuum* **86** 614
[13] Cartry G, Duten X and Rousseau A 2006 *Plasma Sources Sci. Technol.* **15** 479
[14] Lopaev D V, Malykhin E M and Zyryanov S M 2011 *J. Phys. D: Appl. Phys.* **44** 015201
[15] Conway J, Kechkar S, O'Connor N, Gaman C, Turner M M and Daniels S 2013 *Plasma Sources Sci. Technol.* **22** 045004
[16] Walkup A E, Saenger K L and Selwyn G S 1986 *J. Chem. Phys.* **84** 2668
[17] Katsch H M, Tewes A, Quandt E, Goehlich A, Kawetzki T and Döbele H F 2000 *J. Appl. Phys.* **88** 6232
[18] Ivanov V V, Klopovskiy K S, Lopaev D V, Rakhimov A T and Rakhimova T V 2000 *Plasma Physics Reports* **26** 980
[19] Lopaev D V, Volynets A V, Zyryanov S M, Zotovich A I and Rakhimov A T 2017 *J. Phys. D: Appl. Phys.* **50** 075202
[20] Granier A, Chéreau D, Henda K, Safari R and Leprince P 1994 *J. Appl. Phys.* **75** 104
[21] Laher R R and Gilmore F R 1990 *J. Phys. Chem. Ref. Data* **19** 277
[22] Tayal S S and Zatsarinny O 2016 *Phys. Rev. A* **94** 042707
[23] Dobele H F, Mosbach T, Niemi K and Schulz-von der Gathen V 2005 *Plasma Sources Sci. Technol.* **14** S31
[24] Niemi K, Schulz-von der Gathen V and Dobele H F 2005 *Plasma Sources Sci. Technol.* **14** 375
[25] Niemi K, Schulz-von der Gathen V and Dobele H F 2001 *J. Phys. D: Appl. Phys.* **34** 2330
[26] Goehlich A, Kawetzki T and Dobele H F 1998 *J. Chem. Phys.* **108** 9362
[27] Britun N, Belosludtsev A, Silva T and Snyders R 2017 *J. Phys. D: Appl. Phys.* **50** 075204
[28] van Gessel A F H , van Grootel S C, Bruggeman P J 2013 *Plasma Sources Sci. Technol.* **22** (2013) 055010
[29] Schmidt J B, Sands B, Scofield J, Gord J R and Roy S 2017 *Plasma Sources Sci. Technol.* **26** 055004
[30] Schmidt J B, Roy S, Kulatilaka W D, Shkurenkov I, Adamovich I V, Lempert W R and Gord J R *J. Phys. D: Appl. Phys.* **50** (2017) 015204
[31] Sousa J S and Puech V 2013 *J. Phys. D: Appl. Phys.* **46** 464005
[32] Cartry G, Magne L and Cernogora G 1999 *J. Phys. D: Appl. Phys.* **32** L53

[33] Booth J P, Joubert O, Pelletier J and Sadeghi N 1991 *J. Appl. Phys.* **69** 618
[34] Niemi K, O'Connell D, de Oliveira N, Joyeux D, Nahon L, Booth J P and Gans T 2013 *Appl. Phys. Lett.* **103** 034102
[35] Dedrick J, Schröter S, Niemi K, Wijaikhum A, Wagenaars E, de Oliveira N, Nahon L, Booth J P, O'Connell D and Gans T 2017 *J. Phys. D: Appl. Phys.* **50** 455204
[36] Harris S J and Weiner AM 1981 *Opt. Lett.* **6** 142
[37] Gupta M, Owano T, Baer D and O'Keefe A 2006 *Appl. Phys. Lett.* **89** 241503
[38] Hancock G, Peverall R, Ritchie G A D and Thornton L J 2007 *J. Phys. D: Appl. Phys.* **40** 4515
[39] Teslja A and Dagdigian P J 2004 *Chem. Phys. Lett.* **400** 374
[40] Peverall R, Rogers S D A and Ritchie G A D 2020 *Plasma Sources Sci. Technol.* **29** 045004
[41] Baluja K L and Zeippen C J 1988 *J. Phys. B* **21** 1455
[42] Badger R M, Wright A C and Whitlock R F 1965 *J. Chem. Phys.* **43** 4345
[43] Newman S M, Orr-Ewing A J, Newnham D A and Ballard J 2000 *J. Phys. Chem. A* **104** 9467
[44] Williams S, Gupta M, Owano T, Baer D S, O'Keefe A, Yarkony D R and Matsika S 2004 *Opt. Lett* **29** 1066
[45] Foldes T, Cermak P, Macko M, Veis P and Macko P 2009 *Chem. Phys. Lett.* **467** 233
[46] Williams S, Popovic S and Gupta M 2009 *Plasma Sources Sci. Technol.* **18** 035014
[47] Pazyuk V S, Podmar'kov Yu P, Raspopov N A and Frolov M P 2001 *Quantum Electronics* **31** 363
[48] Ogawa S and Ogawa M 1975 *Can. J. Phys.* **53** 1845
[49] Western C M, Booth J P, Chatterjee A and de Oliveira N 2020 *Molecular Physics* e1741714
[50] Gousset G, Panafieu P, Touzeau M and Vialle M 1987 *Plasma Chemistry and Plasma Processing* **7** 409
[51] Klopovskiy K S, Lopaev D V, Popov N A, Rakhimov A T and Rakhimova T V *J. Phys. D: Appl. Phys.* **32** 3004
[52] Crannage R P, Dorko E A, Johnson D E and Whitefield P D 1993 *Chem. Phys.* **169** 267
[53] Lopaev D V, Malykhin E M and Zyryanov S M 2011 *J. Phys. D: Appl. Phys.* **44** 015202
[54] Gibson S T, Gies H P F, Blake A J, McCoy D G and Roger P J 1983 *J. Quant. Spectrosc. Radiat. Transfer* **30** 385
[55] Zyryanov S M and Lopaev D V 2007 *Plasma Physics Reports* **33** 510
[56] Nahon L, de Oliveira N, Garcia G, Gil J F, Pilette B, Marcouille O, Lagarde B and Polack F 2012 *J. Synchrotron Rad.* **19** 508
[57] Hudson R D, Carter V L and Stein J A *J. Geophys. Res.* 1966 **71** 2295
[58] Zatsarinny O, Wang Y and Bartschat K 2014 *Phys. Rev. A* **89** 22706
[59] Dvoryankin A N, Ibragimov L B, Kulagin Yu A and Shelepin L A 1987 *Plasma Chemistry* ed. B.M. Smirnov, Energoatomizdat, Moscow **14** (1987)
[60] McEwan M J and Phillips L F 1975 *Chemistry of the Atmosphere* (New York: Wiley)
[61] Becker K H, Groth W and Schurath U 1972 *Chem. Phys. Lett.* **14** 489
[62] Marinov D, Guerra V, Guaitella O, Booth J P and Rousseau A 2013 *Plasma Sources Sci. Technol.* **22** 055018
[63] Klarenaar, B. L. M., Morillo-Candas, A. S., Grofulović, M., van de Sanden, M. C. M., Engeln, R., & Guaitella, O. (2019) Plasma Sources Science and Technology, 28(3), 035011.
[64] Steinfeld J I, Adler-Golden S M and Gallagher J W 1987 *J. Phys. Chem. Ref. Data* **18** 911
[65] Marinov D, Guaitella O, Booth J P and Rousseau A 2013 *J. Phys. D: Appl. Phys.* **46** 032001
[66] Atkinson R, L.Baulch D, Cox R A, Hampson R F, Kerr J A, Rossi M J and Troe J 1997 *J. Phys. Chem. Ref. Data* **26** 1329
[67] Braginskiy O V, Vasilieva A N, Klopovskiy K S, Kovalev A S, Lopaev D V, Proshina O V, Rakhimova T V and Rakhimov A T 2005 *J. Phys. D: Appl. Phys.* **38** 3609
[68] Zakharov A I, Klopovsky K S, Kovalev A S, Osipov A P, Popov A M, Popovicheva O B, Rakhimova T V, Samorodov V A and Sokolov V A 1988 *Fizika Plazmi* **14** (1988) 327 (Russian)
[69] Zagidullin M V, Pershin A A, Azyazov V N and Mebel A M 2005 *J. Chem. Phys.* **143** 244315